

NIHAO VIII: Circum-galactic medium and outflows - The puzzles of HI and OVI gas distributions

Thales A. Gutcke^{1*}, Greg S. Stinson¹, Andrea V. Macciò^{2,1}, Liang Wang³, Aaron A. Dutton²

¹*Max-Planck-Institut für Astronomie, Königstuhl 17, 69117 Heidelberg, Germany*

²*New York University Abu Dhabi, PO Box 129188, Abu Dhabi, UAE*

³*Purple Mountain Observatory, the Partner Group of MPI für Astronomie, 2 West Beijing Road, Nanjing 210008, China*

19 October 2016

ABSTRACT

We study the hot and cold circum-galactic medium (CGM) of 86 galaxies of the cosmological, hydrodynamical simulation suite NIHAO. NIHAO allows a study of how the $z = 0$ CGM varies across 5 orders of magnitude of stellar mass using OVI and HI as proxies for hot and cold gas. The cool HI covering fraction and column density profiles match observations well, particularly in the inner CGM. OVI shows increasing column densities with mass, a trend seemingly echoed in the observations. As in multiple previous simulations, the OVI column densities in simulations are lower than observed and optically thick HI does not extend as far out as in observations. We take a look at the collisional ionisation fraction of OVI as a function of halo mass. We make observable predictions of the bipolarity of outflows and their effect on the general shape of the CGM. Bipolar outflows can be seen out to around 40 kpc in intermediate and low mass halos ($M_{\text{Halo}} < 10^{11} M_{\odot}$), but outside that radius, the CGM is too well mixed to detect an elongated shape. Larger halos have extended gas discs beyond the stellar disc that dominate the shape of the inner CGM. The simulated CGM is remarkably spherical even in low mass simulations. The chemical enrichment of both halo and disc gas follow expected increasing trends as a function of halo mass that are well fit with power laws. These relations can be used in non-hydrodynamic models, such as semi-analytic models.

Key words:

1 INTRODUCTION

The gas surrounding galaxies, the “circum-galactic medium” (CGM), plays a major role in galaxy formation and evolution. Gas flows into the bottom of potential energy wells and turns into stars to create galaxies. As gas falls into galaxies, the mass of the dark matter halo determines its velocity and the gas heats to the virial temperature. Rees & Ostriker (1977) showed that the cooling time of the CGM gas determines how much gas cools onto the galaxy, which corresponds to the mass scales at which galaxies form.

Theorists are still working out the details of the geometry of that collapse. White & Rees (1978) included dark matter in the collapse and introduced the idea of hierarchical merging to form the most massive halos. Kereš et al. (2005) pointed out that when galaxy masses are low, gas

first cools onto filaments before flowing into galaxies along those narrow paths. Birnboim & Dekel (2003) showed that as the galaxy increased in mass, those filaments would shock near the virial radius and the CGM would cut off the cold gas supply to the galaxy. The shocking of accreting gas is one of the many attempts at an explanation of why star formation becomes so inefficient in galaxies more massive than the Milky Way.

In such models, a large fraction of the baryons in galaxies around and above $10^{11.5} M_{\odot}$ in halo mass is distributed in the CGM. However, since it is spread out over such a large volume it is diffuse enough that it does not emit much radiation. What radiation is emitted comes out at hard to observe energies like X-rays (see e.g. White & Frenk 1991; Crain et al. 2010). It is thus incumbent on modelers to make predictions about the chemical phase, orientation and shapes of the CGM in their models.

Fortunately, observers can detect diffuse gas in absorp-

* thales@mpia.de

tion if a bright source like a quasar lies behind it. Many absorption lines useful for diagnostics are in the UV portion of the spectrum. Thus, it is easiest to study the CGM at high redshifts, such that the lines redshift into the optical portion of the spectrum (e.g. Cowie & Songaila 1995; Schaye et al. 2003; Hennawi et al. 2006; Steidel et al. 2010; Rudie et al. 2012; Lehner et al. 2014).

UV spectrographs were added to the *Hubble Space Telescope* (HST), enabling studies of the low redshift CGM (e.g. Thom & Chen 2008; Tripp et al. 2008; Prochaska et al. 2011). The *Cosmic Origins Spectrograph* (COS) added far-UV sensitivity and made studies of the low redshift CGM easier.

The COS-Halos project focused on studying the CGM surrounding a large sample of $\sim L^*$ galaxies (Tumlinson et al. 2013). Danforth et al. (2014) also studied the low redshift inter-galactic medium (IGM). COS-Halos studied OVI as one of its highly ionized species. Oxygen is collisionally ionised to OVI in gas between $10^5 < T/K < 10^6$. It is also possible for lower temperature gas to be photoionised to OVI by an external radiation field. Oxygen is produced primarily in type II supernovae (SNII) and can flow out of the galaxy with the galactic wind. Thus, OVI can be either a tracer of warm/hot gas in the CGM or a cooler phase that may have flowed out in the wind.

Tumlinson et al. (2011) found OVI detections (their column density detection limit being $N_{\text{OVI}} \gtrsim 10^{14} \text{cm}^{-2}$) in the majority of their 30 observed star forming galaxies, but in none of their sample of red galaxies. In galaxies with OVI detections, it was extended in projection out to 300 kpc, beyond even the virial radius. Making typical assumptions about the metallicity ($0.5 Z_{\odot}$), abundance ratios (solar), and ionization field shining on the CGM leads to high oxygen masses in the CGM, comparable to the amount of oxygen found in the Milky Way disc (Tumlinson et al. 2011; Peebles et al. 2014).

Detailed examination of the absorption line profiles showed hints of components with narrow lines embedded inside broader overall profiles (Tripp et al. 2008; Thom & Chen 2008). These tentative findings hint towards OVI being cooler than expected by collisional ionisation models and generally more consistent with being photoionised.

One surprising result of COS-Halos was that a large fraction of the CGM mass is cool and in a low ionization state. The gas also appears to be in dense knots that are not in hydrostatic equilibrium with their surroundings (Werk et al. 2014). How such gas is supported in the CGM remains a mystery.

Local L^* galaxies are not the only place a surprising amount of cool gas has been found (for other places, see Rudie et al. 2012; Martin et al. 2012; Prochaska et al. 2013; Crighton et al. 2013).

Several studies have looked at the HI covering fraction at a variety of masses throughout cosmic time (Rudie et al. 2013; Prochaska et al. 2014). Commonly, they report the fraction of sight lines in which HI is detected. Fumagalli et al. (2014) provides a nice summary. While models generally predict that the CGM of luminous galaxies (in modelling generally assumed to be the more massive galaxies) is comprised of more hot gas, the observations find higher HI covering fractions of the CGM surrounding more luminous galaxies.

Some work has also been focused on understanding the geometrical extent of the CGM. Bordoloi et al. (2014) present an investigation of the geometry of cool outflows traced by MgII in the absorption line spectra of 486 zCOSMOS galaxies. Splitting their sample by inclination, they find a higher equivalent width out to 40-50 kpc for galaxies with near face on inclination than for edge on galaxies. They take this to be indicative of bipolar outflows perpendicular to the plane of the disc, since absorption spectra will capture the outflowing component face on more strongly than edge on. Kacprzak et al. (2015), using OVI absorption lines, present a bimodality in the azimuthal angle distribution around 53 HST-imaged galaxies. They conclude that this bimodality is consistent with minor-axis driven outflows and that OVI is not mixed throughout the CGM.

1.1 Numerical predictions and observations

Galaxy formation models have used star formation feedback in an attempt to explain the low efficiency of star formation in galaxies (Springel & Hernquist 2003; Murray et al. 2005; Oppenheimer & Davé 2006; Dalla Vecchia & Schaye 2008; Davé et al. 2011; Hopkins et al. 2012; Puchwein & Springel 2013; Vogelsberger et al. 2013; Kannan et al. 2014). Stellar-driven winds could not only deplete the central galaxy of gas, its fuel for star formation, but also transport metal-enriched gas to large distances from the stars (e.g. Aguirre et al. 2001; Theuns et al. 2002; Davé & Oppenheimer 2007; Cen & Chisari 2011; Christensen et al. 2015).

Numerical simulations commonly use one of two prescriptions to model outflows: kinetic (Springel & Hernquist 2003; Davé & Oppenheimer 2007; Oppenheimer et al. 2010; Ford et al. 2015; Suresh et al. 2015) and thermal (Stinson et al. 2006; Dalla Vecchia & Schaye 2012; Shen et al. 2012; Hummels et al. 2013; Schaye et al. 2015; Rahmati et al. 2015). The kinetic model uses a prescription for wind velocities launched from discs. Thermal models make gas around star formation regions hot and allow the supersonic pressure of the hot gas to push gas out of galaxies. Durier & Dalla Vecchia (2012) find that kinetic wind and thermal models converge to the same behavior using correct hydrodynamics.

Kinetic wind models typically turn off hydrodynamics of the wind particles including the recent *Illustris* simulations (Vogelsberger et al. 2014). (But see Schaye et al. (2010) for an implementation of a wind model without hydrodynamical decoupling.) Early studies suggested that without hydrodynamics, such wind prescriptions preserved convergence in results of different resolutions. It is unclear whether such convergence remains in the most recent studies (Vogelsberger et al. 2013).

Many simulated galaxies now broadly match the low redshift stellar mass-halo mass relation (Oppenheimer et al. 2012; Aumer et al. 2013; Stinson et al. 2013; Hopkins et al. 2014; Vogelsberger et al. 2014; Christensen et al. 2015; Schaye et al. 2015; Wang et al. 2015). It is thus worth making a comparison with observations that could lend insight into how the CGM formed and whether it is the repository for the missing baryons in the Universe.

1.1.1 OVI

Hydrodynamical simulations that compare their OVI (e.g.

Hummels et al. 2013; Ford et al. 2015; Suresh et al. 2015) with COS halos observations (Tumlinson et al. 2011) find that their fiducial models produce nearly a dex lower column densities across impact parameters and, when compared, also across luminosities, than the observations.

Our earlier look using a thermal model (Stinson et al. 2012, henceforth S12), showed good agreement with OVI observations, although this was a small sample of two galaxies. The purpose of this work is to expand that sample.

Using an Eulerian grid code, Hummels et al. (2013) studied variations of the CGM with thermal stellar feedback strength. While they were able to match many ion species column densities, they found that OVI presented the biggest challenge. Various strengths of their thermal feedback scheme changed the typical OVI column densities by a half an order of magnitude and the extent of the OVI halo by an order of magnitude. These changes can be attributed to changes in star formation rates due to the availability of gas reservoirs, but also to the differences in outflow strength which effect the metallicity distribution. The feedback prescription in which cooling was suppressed produced results most consistent with observations. Even in that simulation, the simulated OVI column densities remain about half a dex too low. In terms of radial extent, the cooling suppressed feedback also extends as far as the observations. Plenty of oxygen was present in their gaseous halos, but the temperature range for OVI is small enough that not much gas stayed in that state, assuming collisional ionisation dominates.

Focusing on the effect of feedback, Rahmati et al. (2016) used the EAGLE simulation suite to compare their simulated column density distribution functions (CDDFs) of a variety of elements in various ionisation states, including OVI, with observations. They find that the shape and normalisation of the CDDF of OVI both strongly depend on the stellar feedback efficiency due to its effect on the amount of metals produced. But they note that OVI is directly dependent on the strength of the feedback, presumably because the temperature structure effects how much OVI is collisionally ionised

Concentrating on OVI, Suresh et al. (2015) make a detailed study of the offset between the CGM from the *Illustris* simulation and observations. In addition to the nearly order of magnitude offset in column densities, they note that their simulations show a strong correlation between galaxy stellar mass and OVI column density. Their galaxies also show steep column density gradients. Additionally, they model local photoionisation to explain the low OVI column densities in simulations, but only find an effect in the inner 50 kpc of the CGM.

Most recently, Oppenheimer et al. (2016) tested a non-equilibrium ionisation (NEQ) and cooling module using EAGLE zoom simulations. They find that the NEQ does not effect the oxygen ion abundances by more than ~ 0.1 dex. Their fiducial model shows a factor of two too low OVI column densities compared to observations. They argue that the NEQ effects are strongest in shocks and in gas that is exposed to sources fluctuating on a short timescale such as an AGN.

Since S12 did well matching OVI observations, another look with a newer, larger sample of galaxies is worthwhile. The study will allow for a comparison with the trend with stellar mass that Suresh et al. (2015) found.

1.1.2 HI

To begin to understand the large amounts of cool gas surrounding galaxies, Fumagalli et al. (2014) found that the HI covering fractions of their simulated halos with $M_{\text{vir}} < 10^{12} M_{\odot}$ were lower than $z = 2 - 2.5$ observations by a factor of $\sim 30\%$. Moreover, for the halos with $M_{\text{vir}} > 10^{12} M_{\odot}$ they found systematically lower values (factor ~ 3). However, the feedback prescription used in this work was not effective enough, overproducing the amount of stars and underestimating the amount of gas in the halos. It is worth pointing out that this study presented a compilation of previous results. The simulations with some of the highest covering fractions came from the *Eris* simulation (Shen et al. 2012), a simulation run with the same code and cooling modules we use.

Using the FIRE simulation suite, Faucher-Giguère et al. (2015) also studied covering fractions of HI. They found that the physical area the cold gas covers stays roughly constant with cosmic time. Thus, as the virial radius grows, the covering fraction decreases significantly. When they compared with $z \sim 2 - 2.5$ observations they seem to better match the $M_{\text{vir}} < 10^{12} M_{\odot}$ halos but they were still too low for the most massive systems. Originally, these authors claimed that the reason for this could be that their simulations did not include AGN feedback.

In a recent study, Rahmati et al. (2015) examine the HI covering fractions using the EAGLE simulation suite. They approximate the HI ionisation fraction via the same fitting functions as we do (Rahmati et al. 2013) and find close agreement between the Prochaska et al. (2013) and Rudie et al. (2012) observations. They attribute this to their strong stellar and AGN feedback model, although they say that their AGN feedback prescription has a small effect. Their comparison, however, is for larger mass halos, $M_{\text{vir}} > 10^{12.5} M_{\odot}$, captured within their larger simulation volume with an initial gas particle mass of $1.4 \times 10^6 M_{\odot}$.

Even more recently, Faucher-Giguère et al. (2016) argue that, in fact, they can reproduce the observed HI covering fractions for the massive systems without AGN feedback when including strong stellar winds. Their simulations have a gas particle mass of a few times $10^4 M_{\odot}$. This highlights the fact that there is still no general agreement about the HI covering fractions around massive high-redshift galaxies between different state-of-the-art feedback models.

1.1.3 Aim of this paper

In this paper we plan to investigate the CGM properties and characterise the metallicity distribution and shape in Numerical Investigation of a Hundred Astrophysical Objects, NIHAO (Wang et al. 2015) project. The NIHAO simulations are a suite of nearly 100 hydrodynamical, cosmological zoom-in galaxies across a range in mass from $10^5 \lesssim M_{*} / M_{\odot} \lesssim 10^{11}$. The star formation and stellar feedback was developed in the Making Galaxies in a Cosmological Context project (MaGICC Stinson et al. 2013). The NIHAO project builds on this, extending the mass range while keeping the same stellar physics at all scales. Despite the many orders of magnitude between our smallest and largest galaxy, the amount of stellar mass formed in a halo with a given mass agrees with results from abundance match-

ing (Wang et al. 2015). The cold gas mass in the simulated galaxy discs also agree well with observations (Stinson et al. 2015). It is for this reason that the NIHAO sample is an excellent resource for exploring the physics of galaxy formation.

Focusing on the halo mass dependence of properties of the CGM, we will mainly look at low redshifts. This work is an extension of S12 to a large sample of galaxies spanning a wide range in masses. We examine the hard-to-see low density gas surrounding galaxies, in the ensemble of the NIHAO galaxies.

§2 provides an overview of the simulations used to find this result. §3.1 shows the hot gas traced by OVI and how the profiles compare with observations. §3.2 discusses the cold gas density profiles traced by HI and takes a look at the covering fractions of HI, comparing them to observations. §3.3 studies how outflows shape different phases of the CGM. §3.4 looks at the chemical composition of the CGM. §4 provides context for the findings in some recent theoretical models, observations of gas in galaxies, and some possible implications for future observations.

2 SIMULATIONS

The 86 simulations analyzed in this paper are taken from the NIHAO project (Wang et al. 2015). The NIHAO galaxies come from $(15 h^{-1} \text{ Mpc})^3$, $(20 h^{-1} \text{ Mpc})^3$ and $(60 h^{-1} \text{ Mpc})^3$ cubes from Dutton & Macciò (2014). For all work done here, we use the Planck Collaboration et al. (2014) cosmological parameters: $\Omega_m=0.3175$, $\Omega_\Lambda=0.6825$, $\Omega_b=0.049$, $H_0 = 67.1 \text{ km s}^{-1}\text{Mpc}^{-1}$, $\sigma_8 = 0.8344$. The virial mass, M_{vir} , of each halo is defined as the mass of all particles within a sphere containing $\Delta = 200$ times the cosmic critical matter density. The virial radius, R_{vir} , and the virial temperature, T_{vir} , are defined accordingly.

2.1 ESF-Gasoline2

We use the N-body smoothed particle hydrodynamics (SPH) solver GASOLINE (Wadsley et al. 2004) with the modified version of hydrodynamics described in Keller et al. (2014). Their modified version of hydrodynamics removes spurious numerical surface tension and improves multiphase mixing. This arises from the P/ρ^2 calculation as proposed by Ritchie & Thomas (2001), although we do not use densities calculated using equal pressure.

We refer to our version as ESF-GASOLINE2. Instead of the Keller et al. (2014) superbubble feedback, we use the “early stellar feedback” (ESF) model that is described below.

Our simulations use the metal diffusion as described in Wadsley et al. (2008), but we do not use the diffusion of thermal energy between particles, because it is incompatible with the blastwave feedback that delays cooling.

ESF-GASOLINE2 also uses the timestep limiter (Saitoh & Makino 2009) which allows cool particles to behave correctly when a hot blastwave hits them. ESF-GASOLINE2 uses the Wendland $C2$ function for its smoothing kernel (Dehnen & Aly 2012), helping to avoid pair instabilities. The treatment of artificial viscosity has been modified to use the signal velocity as in Price (2008).

The cooling is as described in Shen et al. (2010) and

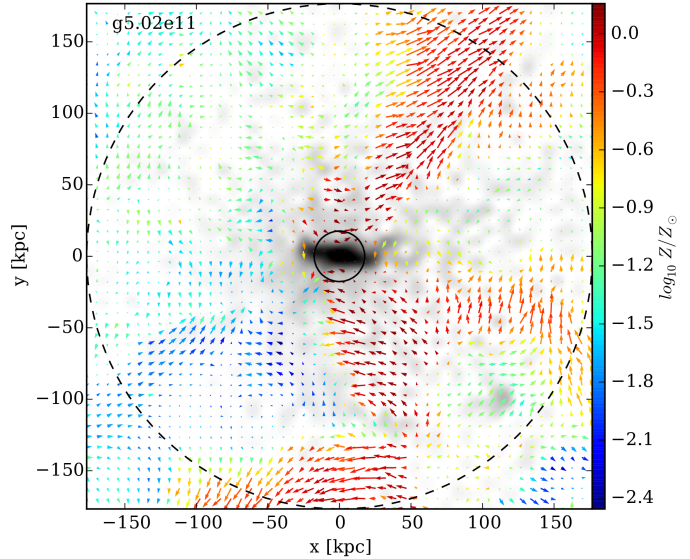


Figure 1. Edge on view of the velocity field in slice $R_{\text{vir}} \times R_{\text{vir}} \times 2 \text{ kpc}$ for one NIHAO galaxy at $z = 0$, g5.02e11. Colors indicate the average metallicity, $\log Z/Z_\odot$, while the grey shaded areas show mean gas density in the slice. The virial radius and 10% of it are shown by the dashed and solid circles, respectively. Metal-rich inflows and outflows can be traced approximately perpendicular to the plane of the disc.

was calculated using CLOUDY (version 07.02; Ferland et al. (1998)) tables that include photoionization and heating from the Haardt & Madau (2005) UV background, Compton cooling, and hydrogen, helium and metal cooling from 10 to 10^9 K. In the dense, interstellar medium gas we do not impose any shielding from the extragalactic UV field as the extragalactic field is a reasonable approximation in the interstellar medium.

2.2 Star Formation and Feedback

The NIHAO simulations use the star formation recipe described in Stinson et al. (2006) that we summarize here. Stars form from cool ($T < 15,000 \text{ K}$), dense gas. The metal cooling readily produces dense gas, so the star formation density threshold is set to the maximum density at which gravitational instabilities can be resolved, $\frac{50m_{\text{gas}}}{\epsilon_{\text{gas}}^3} (n_{\text{th}} > 10 \text{ cm}^{-3})$, where m_{gas} is the gas particle mass and ϵ_{gas} is the gravitational softening of the gas. Such gas is converted to stars according to the equation

$$\frac{\Delta M_\star}{\Delta t} = c_\star \frac{M_{\text{gas}}}{t_{\text{dyn}}}. \quad (1)$$

Here, ΔM_\star is the mass of the star particle formed, Δt is the timestep between star formation events, $8 \times 10^5 \text{ yr}$ in these simulations, and t_{dyn} is the gas particle’s dynamical time. c_\star is the efficiency of star formation, i.e. the fraction of gas that will be converted into stars during t_{dyn} .

The simulations use the same stellar feedback as described in Stinson et al. (2013). In this scheme, the stars feed energy back in two epochs. The first epoch, “pre-SN feedback” (ESF), happens before any supernovae explode. It represents stellar winds and photoionization from the

bright young stars, and the efficiency parameter is set to $\epsilon_{ESF}=13\%$. Radiative cooling is left *on* for the pre-SN feedback.

The second epoch starts 4 Myr after the star forms, when the first supernovae start exploding. Only supernova energy is considered as feedback in this second epoch. Stars $8 M_{\odot} < M_{*} < 40 M_{\odot}$ eject both energy and metals into the interstellar medium gas surrounding the region where they formed. Supernova feedback is implemented using the blastwave formalism described in Stinson et al. (2006). Since the gas receiving the energy is dense, it would quickly be radiated away due to its efficient cooling. For this reason, cooling is delayed for particles inside the blast region for 30 Myr. This time is extended if a particle resides in the blast region of multiple supernovae.

2.3 Calculating HI fractions

Unlike S12, which used an optically thin CLOUDY calculation to compute the HI neutral fraction, we use an analytic fits to radiative transfer calculations presented in Rahmati et al. (2013). Rahmati et al. (2013) post-processed SPH simulation using the radiative transfer code TRAPHIC detailed in Pawlik & Schaye (2008) and Pawlik & Schaye (2011). They show that the fitting functions, which include self-shielding density thresholds dependent on density and redshift, produce results in excellent agreement with their full radiative transfer calculations.

The CLOUDY calculation used in S12 found hydrogen ionization fractions as high as 0.3 even at densities above 0.1 cm^{-3} .

Table 2 in Rahmati et al. (2013) presents self-shielding density thresholds at discrete redshifts and for different cosmic ionization backgrounds. We calculate the self-shielding density threshold by interpolating between the redshift values for the Haardt & Madau (2001) cosmic ionizing UV background. The Rahmati et al. (2013) density threshold rises from $1.1 \times 10^{-3} \text{ cm}^{-3}$ at $z = 0$ to 8.7×10^{-3} at $z = 2$ before decreasing to higher redshifts.

3 RESULTS

Our study of the CGM starts with a visual inspection of warm and cool gas in ionization lines that are commonly observed, OVI and HI. For the higher mass galaxies, we compare these with observations. Then we investigate trends of the shape and extent of the CGM as a function of total galaxy mass.

In Fig. 1 we show a $z = 0$ slice of one (arbitrary) NIHAO galaxy viewed side-on (thickness = 2 kpc) to give us a qualitative impression of gas flows in the halo. The gray shading represents gas density inside the slice. We overlay the gas velocity field directions as arrows. Arrow length scales with velocity and arrow color shows the average metallicity of the gas in units of solar metallicity. The dashed black line encompasses the virial radius. Large, metal-rich ($\log Z/Z_{\odot} > -0.4$) inflows are visible in the lower right hand corner, while at the same time metal-rich outflows are being driven in the upper right hand corner.

3.1 Hot gas

Although this analysis uses 86 galaxies of the NIHAO suite, Fig. 2 shows column density maps of OVI for the same 30 NIHAO galaxies shown in Wang et al. (2015). The OVI mass is calculated per particle as in S12 using 1 cm thick gas slabs in Cloudy (v10.0 last described in Ferland et al. (1998)). The gas is radiated with a Haardt & Madau (2005) UV radiation field evaluated at $z = 0$. The resulting OVI mass is smoothed using the smoothing kernel and then the images are created as projections of the OVI mass through the entire zoom region, a $\sim 4 \text{ Mpc}$ line-of-sight.

The 30 OVI maps in Fig. 2 are ordered by M_{vir} and range from $\approx 10^{10} - 10^{12} M_{\odot}$. The x and y axes are scaled to show the gas halos out to $2R_{\text{vir}}$. Qualitatively, Fig. 2 shows the OVI column and its extent scales with M_{vir} : the small galaxies are practically devoid of OVI, while more massive galaxies show observable OVI column densities out past $2R_{\text{vir}}$.

To compare the galaxies with observations, we use the column density maps as though each position was a QSO sightline to make a sample of thousands of sightlines.

Since the observed samples necessarily combine observations from a variety of galaxies, Fig. 3 and Fig. 4 show combinations of column density profiles of all 86 simulated galaxies. All the sightlines from each group of simulations are combined. Fig. 3 shows the median OVI column density as a function of impact parameter b normalised to each respective virial radius (left panels). The impact parameter directly is shown in the left panels of Fig. 4 as the black solid line. The green-gray shaded area shows the 5-95 percentile range of our data. Individual galaxy profiles are shown in fig. A1 of the appendix for the same 30 galaxies as Fig. 2. The functional form of the combined profiles in Fig. 4 is very similar to the individual galaxy profiles seen in Fig. A1. This indicates that the galaxy-to-galaxy variations are small and that the combined trends mainly show the variation in profiles. Solely the galaxies with the smallest luminosities ($L < 0.002L^*$, the profiles without observational data in Fig. A1) show a larger galaxy-to-galaxy scatter. These are neither compared to observations, nor included in Fig. 4.

Observed data from galaxies of similar luminosities are overlaid on top of the simulated columns of Fig. 4, according to the luminosity ranges used in Prochaska et al. (2011), $0.01L^* < L < 0.1L^*$, $0.1L^* < L < 1L^*$ and $L > 1L^*$. In the luminosity range $0.1L^* < L < 1L^*$, data from Tumlinson et al. (2011) as gray circles. Luminosities are calculated for the simulated galaxies using Padova simple stellar populations (Marigo et al. 2008; Girardi et al. 2010). L^* is taken as $M_V = -21.12$ as reported in Prochaska et al. (2011). Tumlinson et al. (2011) gives SDSS r -band galaxy magnitudes; we use $M_r = -20$ for L^* . While the COS-Dwarfs project (Bordoloi et al. 2014) observed galaxies of similar luminosity as our lowest mass simulations, they have yet to publish OVI columns.

When exact data values are given, they are shown as filled black circles. Upper limits are shown as downward pointing triangles, and lower limits are shown as upward pointing triangles.

No observations are shown in Fig. 3 since neither the virial radii nor the stellar masses are available for the observed galaxies.

!htbp

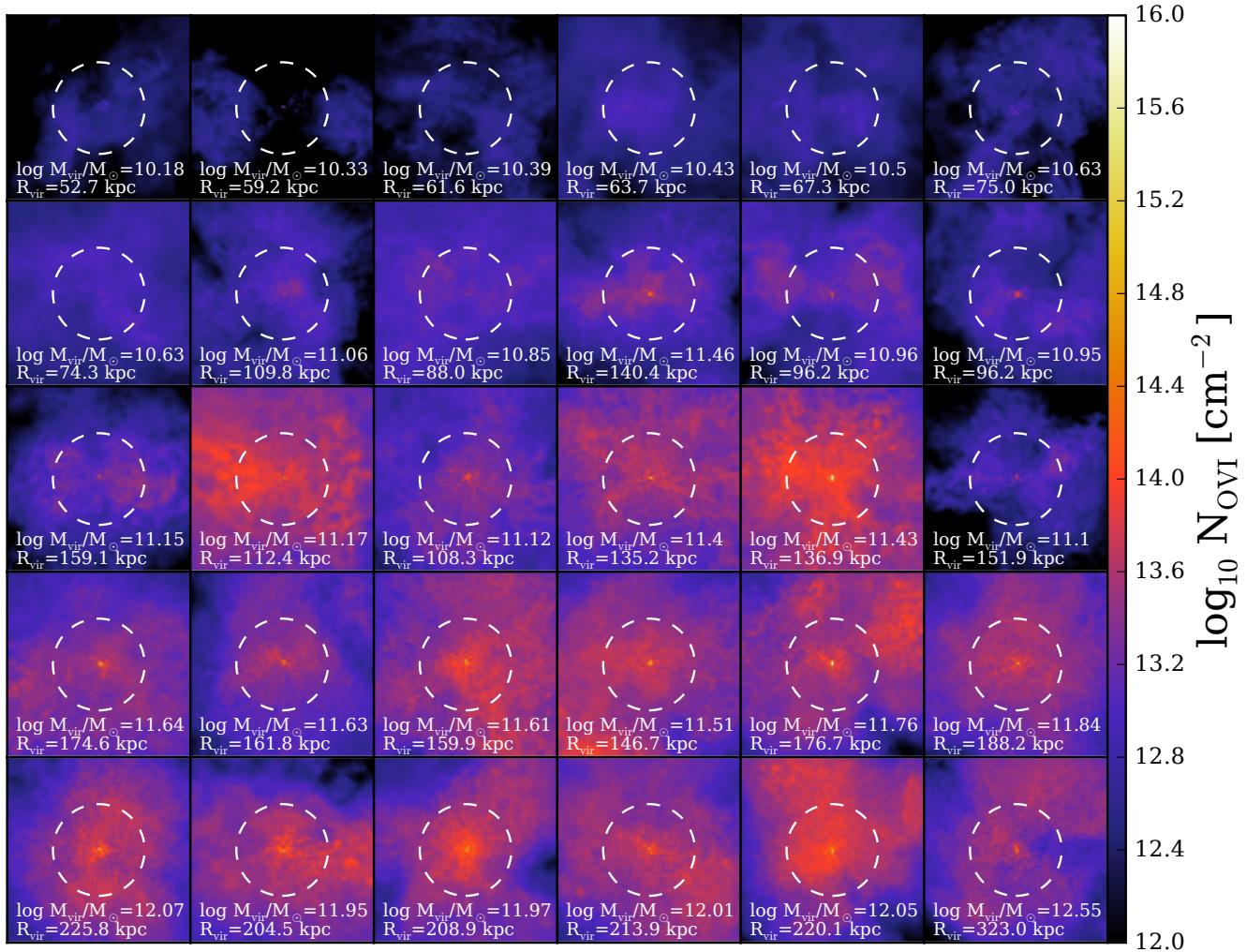


Figure 2. OVI column density maps for the same 30 NIHAO galaxies as in Wang et al. (2015). The CGM images are oriented such that the discs are face-on. Each image is $2R_{\text{vir}}$ on each side, while the dashed white circle indicates the virial radius.

The general trend of increasing column density with increasing M_{star} (so also total luminosity) is apparent. For this analysis, we will focus on the $0.1 < L/L^* < 1$ range, since many of the observations in the lower luminosity bins are only upper limits, and the sample size is mainly limited in the higher luminosity bin. In the $0.1 < L/L^* < 1$ range, the simulations are about half a dex lower than the median of the observations. Such an offset is typical of comparisons of OVI observations with simulations (Ford et al. 2015; Humels et al. 2013; Suresh et al. 2015). Various causes are mentioned, among them that the oxygen, which seems available in sufficient amounts, is not in the correct ionisation state. Assuming collisional ionisation dominates, this points to a problem with the thermal structure of the CGM produced in hydrodynamical simulations. Further discussion of this in §4.

There are two significant differences that could explain the apparent discrepancy between the NIHAO sample and analysis of S12. First, the NIHAO sample is much larger than the 2 galaxies shown in S12. In S12, only the brighter galaxy well matched the observations.

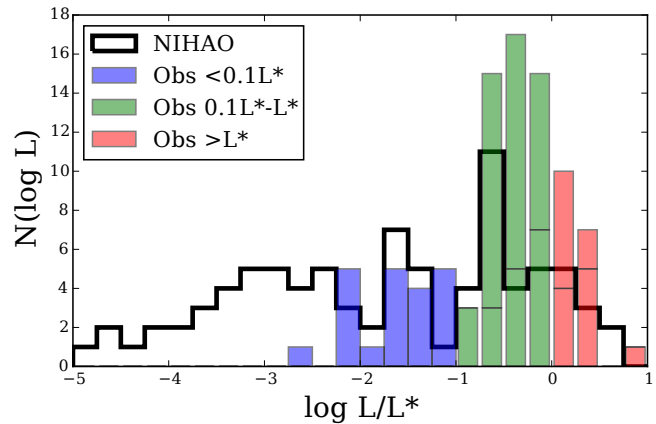


Figure 5. Luminosity distribution of NIHAO galaxies is presented as a black line. The coloured bars (blue, green, red) show the distribution of observations from Prochaska et al. (2011) and Tumlinson et al. (2011).

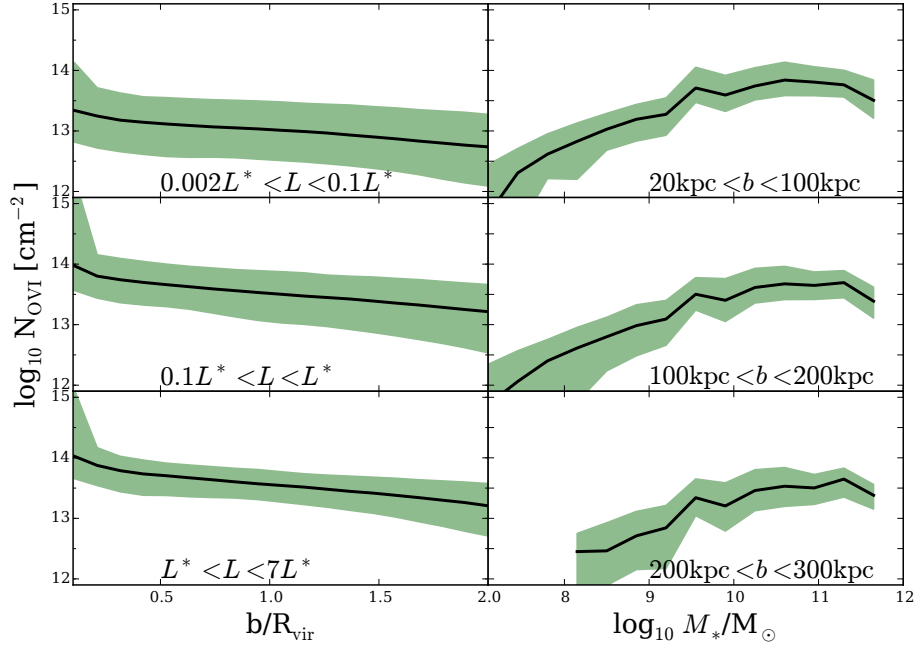


Figure 3. OVI column density ($z = 0$) as a function of: impact parameter normalized to the virial radius (left panels) and stellar mass (right panels). All sight lines from face-on and edge-on for every NIHAO galaxy are included. The black solid line shows the median column density at $z = 0$, while the green band shows the 5-95 percentile range. In the left panels, the column densities are divided between three luminosity bins: $L < 0.1L^*$ (upper panel), $0.1L^* < L < 1L^*$ (middle panel) and $L > 1L^*$ (lower panel). In the right panels, the column densities are divided between radial bins: $20 < b/\text{kpc} < 100$ (upper panel), $100 < b/\text{kpc} < 200$ (middle panel) and $b > 200$ kpc (lower panel).

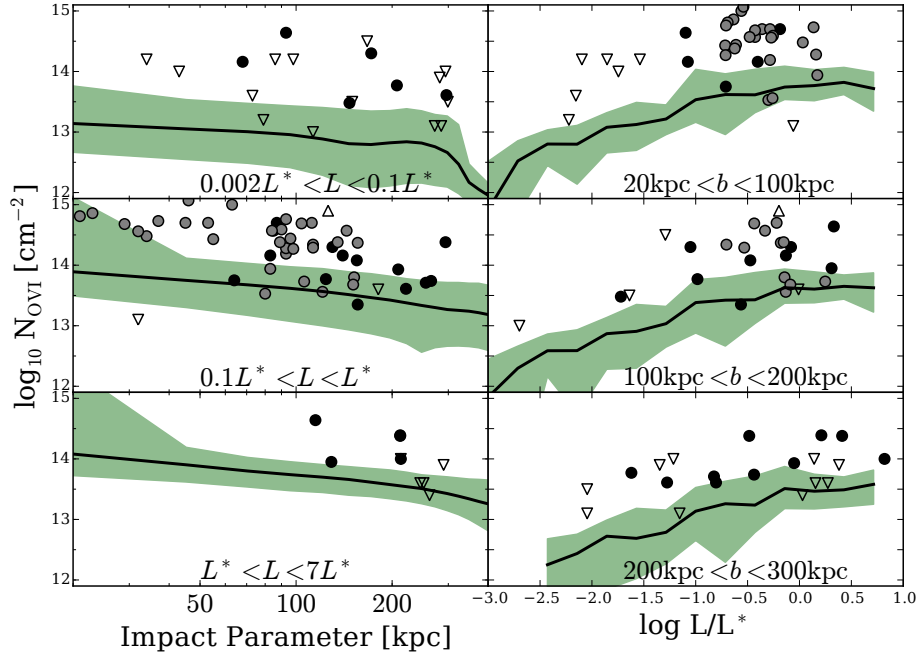


Figure 4. OVI column density ($z = 0$) as a function of: impact parameter (left panels) and luminosity (right panels). The simulations and binning are the same as in Fig. 3 above. Observational data from Prochaska et al. (2011) are shown as black circles. Tumlinson et al. (2013) data is shown as gray circles. Non-detected upper and optically thick lower limits are shown as upward and downward facing open triangles, respectively. Observational points are only shown in the lower panels, since the virial radii and stellar masses of the observations are not known.

Fig. 5 shows that NIHAO samples the lower half of the $0.1L^* < L < 1L^*$ bin more than the OVI observations, which are mostly in the upper half of the bin. The right panels of Fig. 4 are helpful to make this comparison. They show that at common projection radii and galaxy luminosity, NIHAO galaxies indeed have lower OVI column densities.

Another difference between NIHAO and S12 is the stellar feedback. S12 used a slightly different version of hydrodynamics that required stronger stellar feedback to reduce star formation enough to fit on the stellar mass–halo mass relation. S12 and Hummels et al. (2013) showed that more stellar feedback add OVI to the CGM. We discuss in §4 various solutions to this problem. While the discrepancy is unwelcome, it is not so large that it precludes drawing other useful information about the properties of the CGM in simulations.

For example, the OVI column density profiles in the left panel of Fig. 4 are remarkably flat. From the centre out to 250 kpc, N_{OVI} varies less than 0.2 dex in the $0.002 < L/L^* < 0.1$ range. In both $0.1 < L/L^* < 1$ and $1 < L/L^* < 10$ luminosities, N_{OVI} slowly, but steadily declines 0.7 dex over 300 kpc. S12 and Hummels et al. (2013) both showed that with lower feedback, the OVI does not extend to high radii. However, with sufficient feedback to match the stellar mass a galaxy should have, the OVI extends in a flat distribution as far as the observations. Suresh et al. (2015) shows a much steeper profile, close to a 2 dex decline in N_{OVI} over 300 kpc in *Illustris*. Ford et al. (2015) shows little decline to 150 kpc in either their energy dependent or constant wind model. But we note that the Ford et al. (2015) analysis compares equivalent widths instead of column densities.

To examine the question of how much OVI depends on stellar mass or luminosity, the right panels of Fig. 3 and Fig. 4 show column density as a function of stellar mass and galaxy luminosity, respectively, binned into three ranges of the *impact parameter* b : $20 < b/\text{kpc} < 100$, $100 < b/\text{kpc} < 200$ and $b/\text{kpc} > 200$. The median column density is shown as the black line. The green area outlines the spread between the 5th and 95th percentiles in the 0.25 dex luminosity bins. The simulations follow the general trends of the observations, albeit nearly a dex below the observations in all radial ranges.

The simulations clearly show a correlation between stellar mass and N_{OVI} in Fig. 3. This relation is mirrored in the luminosity trends in Fig. 4. N_{OVI} rises steadily from unobservable to a threshold N_{OVI} around 10^{14} cm^{-2} . The simulations reach the 10^{14} cm^{-2} threshold at higher galaxy luminosities the higher the impact parameter range is, from $10^{-0.5}L^*$ in the central bin, to L^* in the medium distance radius to $> L^*$ for the largest values of b . It makes sense that brighter galaxies that formed more stars have more enriched material further away. The issue with the simulations seems to be that the threshold N_{OVI} is lower than what is observed.

N_{OVI} observations are often interpreted as showing little to no dependence on luminosity. More observations are necessary to make definite statements, but the right panels of Fig. 4 hint at a correlation. To distinguish whether there is a trend or not, more observations are necessary at lower luminosities, since there are very few OVI detections below $0.1L^*$. The trend in the simulations is visible because they predict N_{OVI} below the detectable limit.

3.2 Cold gas

Quasar absorption line spectra also include many low ionization absorption lines that indicate the presence of cool gas. Here, we examine HI as the proxy for cool gas in the simulations. Since hydrogen is so abundant, getting the correct ionization fraction requires following radiative transfer. Rahmati et al. (2013) found that a local self-shielding approximation gives results reasonably consistent with the full radiative transfer solution. We report HI column densities based on Rahmati et al. (2013) and note that this is a different treatment than that used in S12, which used an equilibrium CLOUDY model for determining HI fractions. Details can be found in §2.3.

Fig. 6 shows HI maps at $z = 0$ (blue), $z = 2$ (red), and $z = 3$ (grey) for a representative selection of 10 galaxies spanning the NIHAO mass range. Each image is scaled to be $4 R_{\text{vir}}$ across and along a $\sim 4 \text{ Mpc}$ line-of-sight (A discussion of this is in section 4). We include higher redshift analysis because some of the most surprising results about the CGM are the high covering fractions of low ionisation lines. Such values have been reported at $z > 2$ (Rudie et al. 2013; Prochaska et al. 2014; Crighton et al. 2015).

The white dashed circle is drawn at R_{vir} and the black contours show where $\log N_{\text{HI}} > 17.2$, sometimes used as a limit for where HI is considered optically thick. $\log N_{\text{HI}} > 17.2$ is used as a threshold in Fig. 7 to calculate the covering fractions of HI inside R_{vir} and $2R_{\text{vir}}$ for the three redshifts shown using the entire NIHAO sample. Since covering fraction measurements require many quasar absorption lines, there are only 2 reported observational data points at $z = 2 - 3$. Our estimates are compared with the observations of Rudie et al. (2012), who looked at a sample of Lyman Break Galaxies (LBGs) and Damped Lyman Alphas (DLAs) in the redshift range $z = 2 - 2.5$. LBGs have a higher M_{vir} than nearly every NIHAO galaxy (but for comparisons of larger galaxies simulated with a similar feedback scheme, see Faucher-Giguère et al. 2015; Faucher-Giguère et al. 2016). We also compare to a data point of Prochaska et al. (2013), who measured Lyman limit systems in a redshift range $z = 2 - 2.5$ with the aid of luminous background quasars.

With that caveat, it appears the simulated covering fractions inside R_{vir} reach nearly the level of the Rudie et al. (2012) data point at $z = 3$. However, when comparing with the larger $2R_{\text{vir}}$ measurement, the simulated covering fraction halves. As we will see, observations repeatedly find more cool gas distributed far from galaxies than simulations. In Rudie et al. (2012), the cool gas seems to extend well beyond R_{vir} .

After the galaxies have evolved to $z = 2$, the simulations show about half the covering fractions they did at $z = 3$. So, the simulations show covering fractions less than one half of those found in the observations.

The lowest three panels in Fig. 7 show that the simulations actually maintain a constant optically thick physical area according to the galaxy’s M_{vir} . The blue line in each panel shows the fit to the $z = 0$ data and is repeated in each panel as a reference for the reader. From this, it can be seen that the area covered does not increase much over time and that the covering fractions are decreasing mostly due to the

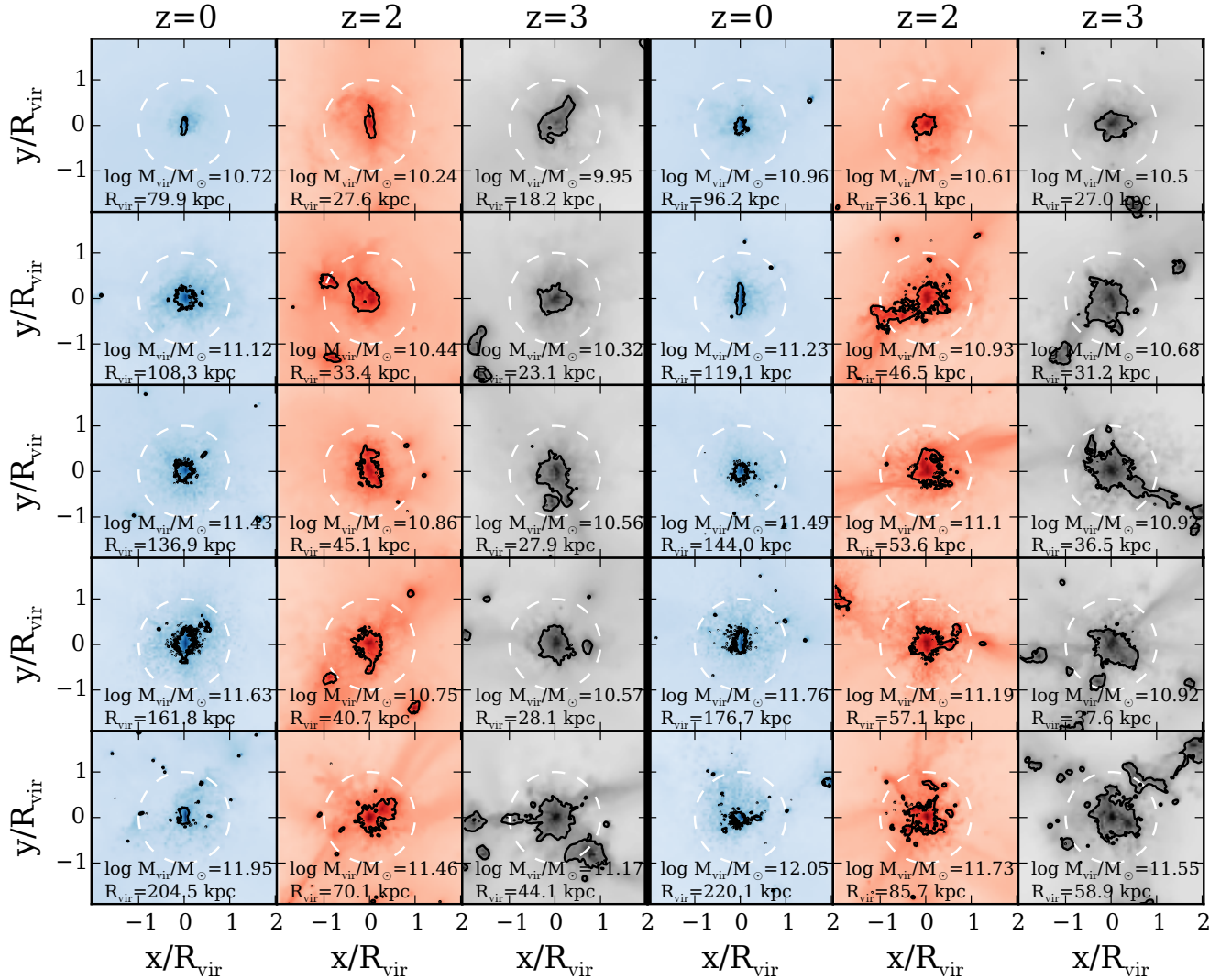


Figure 6. Face-on HI column density maps for 10 NIHAO galaxies. The first and fourth column shows $z = 0$, while the two neighbouring columns show $z = 2$ and $z = 3$, respectively. The black contours indicate the $\log N_{\text{HI}} > 17.2 \text{ cm}^{-2}$ threshold, above which the gas is considered optically thick. Each box is $2R_{\text{vir}}$ on each side, while the dashed white circle indicates the virial radius.

Table 1. Covering fractions of HI for halos with $M_{\text{Halo}} \sim 10^{12} M_{\odot}$ at $z = 2$ and $z = 3$ and for Rudie et al. (2012).

$\log(N_{\text{HI}}/(\text{cm}^{-2}))$	$z=2$		$z=3$		Rudie+2012	Rudie+2012
	$f_{\text{C}}(< R_{\text{vir}})$	$f_{\text{C}}(< 2R_{\text{vir}})$	$f_{\text{C}}(< R_{\text{vir}})$	$f_{\text{C}}(< 2R_{\text{vir}})$	$f_{\text{C}}(< R_{\text{vir}})$	$f_{\text{C}}(< 2R_{\text{vir}})$
> 15.5	$45 \pm 3\%$	$20 \pm 1\%$	$73 \pm 7\%$	$41 \pm 10\%$	$90 \pm 9\%$	$68 \pm 9\%$
> 17.2	$12 \pm 1\%$	$3.8 \pm 0.2\%$	$24 \pm 5\%$	$10 \pm 4\%$	$30 \pm 14\%$	$28 \pm 9\%$
> 19.0	$2.5 \pm 0.2\%$	$0.8 \pm 0.1\%$	$5 \pm 3\%$	$2 \pm 1\%$	$10 \pm 9\%$	$8 \pm 5\%$
> 20.3	$0.8 \pm 0.1\%$	$0.25 \pm 0.04\%$	$1.4 \pm 0.7\%$	$0.5 \pm 0.3\%$	$0_{-0}^{+10}\%$	$4 \pm 4\%$

increasing R_{vir} as the background density decreases and the Universe evolves.

We also compare our most massive systems with further data from Rudie et al. (2012) in table 1. For each covering fraction at different column density thresholds, our $z = 3$ is closer to the observations, but most are still too low by more than 1 sigma. It should be noted that our line-of-sight is limited to the zoom region, $\sim 4 \text{ Mpc}$ which is significantly less than in observations. This biases our column densities

to lower values. Since other simulations have also under-predicted the HI covering fractions, this points to an issue with the amount of HI at larger radii (but see Faucher-Giguere et al. 2016 and Rahmati et al. 2015 for discussion of the effect of feedback strength on HI covering fractions).

Figs. 8 and 9 present the combination of the data from the entire NIHAO sample (86 galaxies at $z = 0$) in the same manner as was done for OVI in Figs. 3 and 4. Again, individual galaxy profiles can be viewed in Fig. A2 of the appendix.

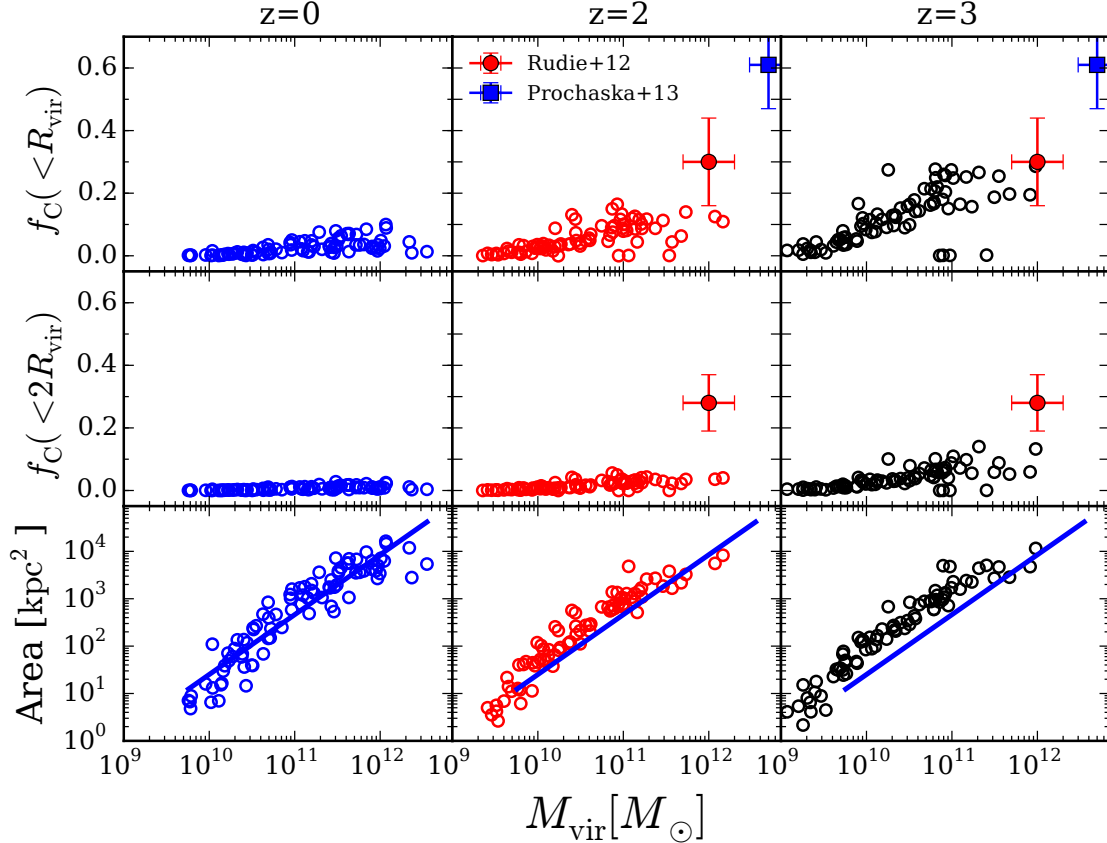


Figure 7. Fraction of area covered by HI with a column density for which $\log N_{HI} > 17.2 \text{ cm}^{-2}$. Upper panels show the projected area fraction inside R_{vir} for $z = 0, 2$ and 3 . Middle panels show the covering fraction in $2R_{vir}$. The red error bars are from observations by Rudie et al. (2012), who observed LBGs in a redshift range $z = 2-2.5$. The blue error bars are from Prochaska et al. (2013) measurements of Lyman limit systems (LLS) via luminous quasi-stellar objects (QSOs). We plot the same observational points on our $z = 2$ and $z = 3$ panels. The middle panels also include an observational point from Rudie et al. (2012) for the fraction inside $2R_{vir}$. The lower panels show the area covered (in kpc^2). The blue line is a power law fit to the $z = 0$ data and overplotted on the $z = 2$ and $z = 3$ panels for reference.

In both panels of Fig. 9, the black line shows the median of the combined data and while the shaded region shows the range of data from the 5th to 95th percentile. In the left panel, column density profiles are combinations of column densities from galaxies broken into three luminosity bins. The simulations show a broader scatter in HI than they did for OVI.

The simulations agree much better with the HI data than they did with the OVI data. In all three luminosity bins, the median column density line goes through the middle of the observations. The simulations have a similar scatter to the observations. One possible exception is the dwarf galaxies ($L < 0.1L^*$), for which there are observations outside 100 kpc that show higher column densities than the simulated column densities.

The right panels of Fig. 9 show how the HI column density varies as a function of galaxy luminosity, split into three impact parameter bins: $20 < b/\text{kpc} < 100$, $100 < b/\text{kpc} < 200$, and $200 < b/\text{kpc} < 300$.

It is clear in Fig. 9 that the scatter of HI columns is largest close to the galaxy. The median HI column density in the simulations increases strongly when going towards

smaller projected radii. This trend goes with galaxy luminosity. In the two inner b bins (two upper right panels of Fig. 9), the simulated median column density generally follows the observations. The column density does not increase as much in the outer two radial b bins. In the 100-200 kpc bin, it appears that the median observed HI column density actually increases. Again, outside 200 kpc, the observed column densities are above the simulation. It seems that the simulations have trouble putting enough cool gas at large distances from galaxies. This could be an improper treatment of the hydrodynamics or an incorrect propulsion of the winds. We discuss reasons for the lack of HI at large distances in §4.2.

3.3 Outflows and shape of the CGM

Since quasars are so rare, it will never be possible to observe the shape of the low density CGM with absorption line studies. However, closer to the disc, integral field unit (IFU) spectrographs are making it possible to map velocity dispersions of gas immediately surrounding galaxies. In recent observational studies (Wild et al. 2014), it has been assumed that an increase in velocity dispersion above and below the plane of

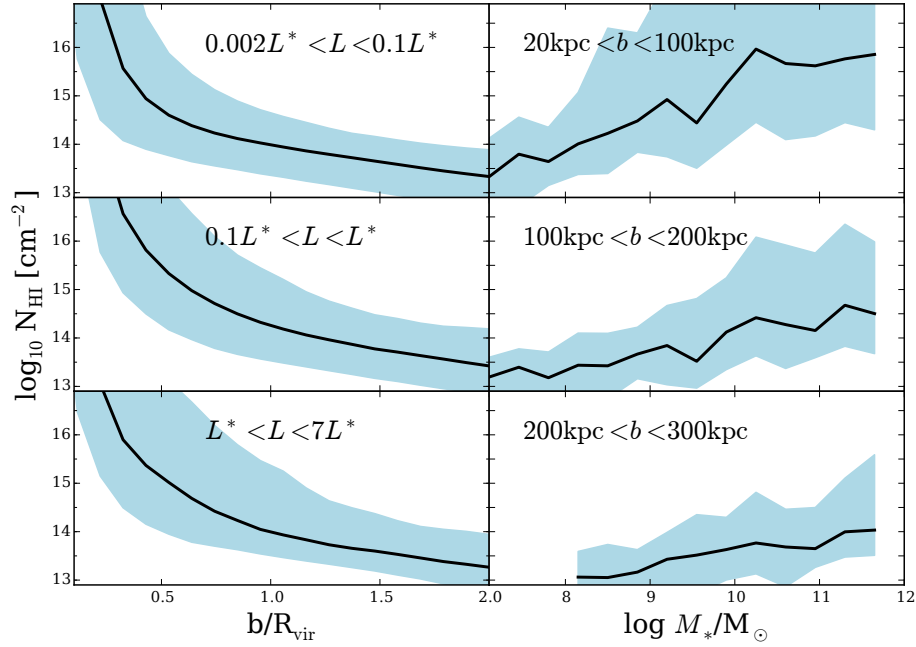


Figure 8. HI column density ($z = 0$) as a function of: impact parameter normalized to the virial radius (left panels) and stellar mass (right panels). All sight lines from face-on and edge-on for every NIHAO galaxy are included. The black solid line shows the median column density at $z = 0$, while the green band shows the 5-95 percentile range. In the left panels, the column densities are divided between three luminosity bins: $L < 0.1L^*$ (upper panel), $0.1L^* < L < 1L^*$ (middle panel) and $L > 1L^*$ (lower panel). In the right panels, the column densities are divided between radial bins: $20 < b/\text{kpc} < 100$ (upper panel), $100 < b/\text{kpc} < 200$ (middle panel) and $b > 200$ kpc (lower panel).

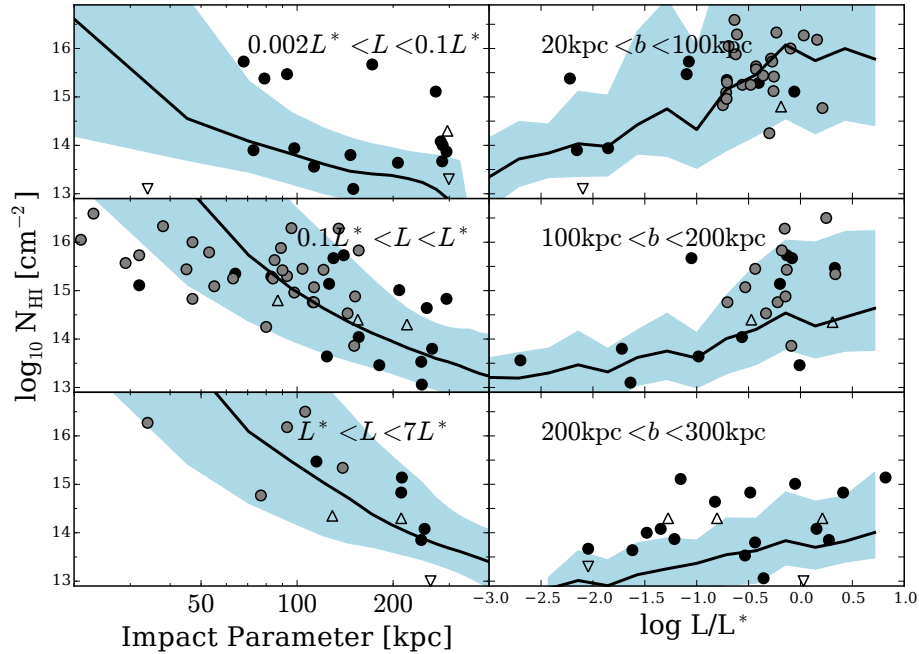


Figure 9. HI column density ($z = 0$) as a function of: impact parameter (left panels) and luminosity (right panels). The simulations and binning are the same as in Fig. 3 above. Observational data from Prochaska et al. (2011) are shown as black circles. Tumlinson et al. (2013) data is shown as gray circles. Non-detected upper and optically thick lower limits are shown as upward and downward facing open triangles, respectively. Observational points are only shown in the lower panels, since the virial radii and stellar masses of the observations are not known.

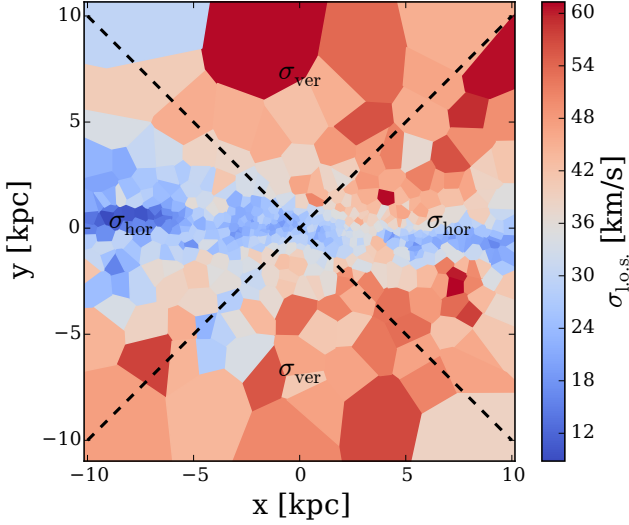


Figure 10. Edge-on velocity dispersion map of NIHAO galaxy, g5.02e11 at $z = 0$. In the tessellation, the disc is apparent as lower line-of-sight (los) velocity dispersion (blue). Above and below the plane of the disc, the los velocity dispersion increases (red). Wild et al. (2014) proposes dividing the velocity dispersion map using the black dashed lines to detect a bipolar outflow. σ_{ver} is the mean velocity dispersion in the triangular regions above and below the disc, while σ_{hor} indicates the mean velocity dispersion in the disc plane.

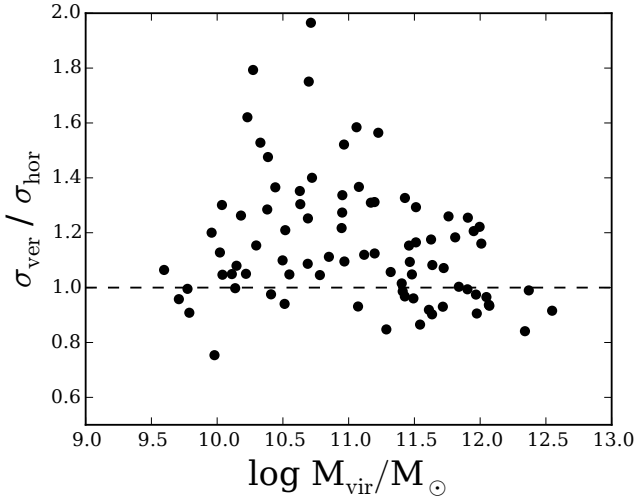


Figure 11. $\langle\sigma_{\text{ver}}\rangle/\langle\sigma_{\text{hor}}\rangle$ as a function of halo mass, M_{vir} . $\langle\sigma_{\text{ver}}\rangle > \langle\sigma_{\text{hor}}\rangle$ in 70% of NIHAO galaxies, which can be interpreted as a preference for outflows to be perpendicular to the disc. Low and high mass galaxies have less clear bipolar outflows than galaxies with masses in the range $10.3 < \log(M_{\text{vir}}/M_{\odot}) < 11.3$. Low feedback efficiency in low mass galaxies and deep potential wells in high mass galaxies limit the amount of gas that escapes perpendicular to the disc.

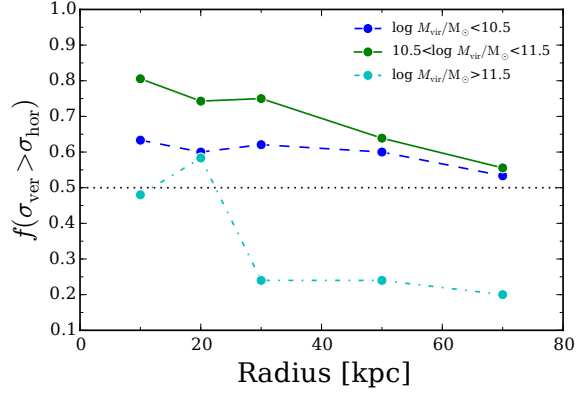


Figure 12. Fraction of all NIHAO galaxies with $\langle\sigma_{\text{ver}}\rangle > \langle\sigma_{\text{hor}}\rangle$ as a function of galaxy radius in three different halo mass ranges, $\log M_{\text{vir}}/M_{\odot} < 10.5$ (blue dashed line), $10.5 < \log M_{\text{vir}}/M_{\odot} < 11.5$ (green solid line) and $\log M_{\text{vir}}/M_{\odot} > 11.5$ (cyan dash-dotted line). The higher fraction of galaxies with $\langle\sigma_{\text{ver}}\rangle > \langle\sigma_{\text{hor}}\rangle$ at small radii indicates that bipolar outflows extend to ~ 40 kpc. The low fractions for the largest halos are due to the extended gas discs that dominate the velocity dispersion in the plane of the discs.

the disc is a dynamical signature of bipolar outflows. Since outflows are expected to create steamers extending radially outward from the nucleus, the line-of-sight velocity dispersion should increase in the presence of a superwind. This is due to the increased line width caused by the bulk motion of the gas toward and away from the observer (Wild et al. 2014). Wild et al. (2014) use this method to study the kinematical structure of the “Mice”, a major merger galaxy pair, and identified strong, galactic scale outflows in one of the “Mice” (NGC 4676A) using the IFU survey CALIFA. Since a pressure driven wind will exit a galaxy in the direction of least pressure (Hayward & Hopkins 2015), we expect outflows to exit our discs in bipolar outflows.

For this study, we make mock IFU observations of the disc edge-on. To this end, we project the galaxy onto the x-y plane and divide the plane into cells of approximately the same number of particles. A Voronoi tessellation is calculated based on the center of mass of each cell and the line-of-sight velocity dispersion is calculated for all particles in each cell. An example of a velocity dispersion map for the inner 10 kpc of a $5 \times 10^{11} M_{\odot}$ galaxy from NIHAO is shown in Fig. 10. The black dashed lines split the map into four triangular areas. The mean velocity dispersion of each of these is calculated. The mean velocity dispersion about the center of mass of the cells in the vertical direction (above and below the disc) is called σ_{ver} . The mean velocity dispersion in the cells along the plane of the disc (left and right) regions is called σ_{hor} .

To understand whether there is an outflow trend with halo mass, Fig. 11 shows the ratio of the mean velocity dispersions in the two directions, $\sigma_{\text{ver}}/\sigma_{\text{hor}}$, inside 10 kpc as a function of M_{vir} . The most significant outflows (i.e. the departure from a ratio of 1) are seen between $10.2 < \log(M_{\text{vir}}/M_{\odot}) < 11$. These are similar masses to where the maximum stellar feedback effects are seen in other studies like Di Cintio et al. (2014) and Tollet et al. (2016), so it is no surprise that the strongest bipolar outflow signal is seen here.

In the lowest mass galaxies, the lack of bipolar signal can be attributed to the lack of star formation. Stars form sporadically at these low masses, so it is unlikely outflows would be detected at the one output when these measurements are made. Few stars have formed over the last several Gyr in these lowest mass simulations. In higher mass galaxies, there is plenty of star formation to potentially drive winds, but wind strengths do not increase so the deepening potential well in more massive galaxies keeps the gas locked inside the disc.

A perfectly isotropic velocity dispersion would not show any of the heightened velocity dispersion in the vertical direction that is seen in Fig. 11. An isotropic distribution would have half the galaxies above and half below 1. Inside 10 kpc, 71% of galaxies have an increased velocity dispersion above and below the plane of the disc relative to around the disc. So, Fig. 12 looks at the fraction as a function of radius for three different halo mass ranges. Both the small ($\log M_{\text{Halo}}/M_{\odot} < 10.5$) and intermediate ($10.5 < \log M_{\text{Halo}}/M_{\odot} < 11.5$) halo mass ranges shows that the velocity dispersion becomes more isotropic as we move out. Bipolar outflows are most visible in intermediate mass galaxies at radii out to around 50 kpc. Beyond 50 kpc, CGM turbulence and galaxy mergers mix the gas such that the bipolarity is no longer visible. The largest halos ($\log M_{\text{Halo}}/M_{\odot} > 11.5$) have a very low dispersion ratio. This is due to the fact that our largest systems are dominated by extended gas discs, which fall into our CGM definition but lie in the plane of the disc.

In the center of the halo ($r \lesssim 50$ kpc), our predictions of the velocity dispersion will depend on our specific thermal feedback prescription, since this is what is driving the outflows. And yet, the feedback strength was calibrated to obtain the correct stellar mass - halo mass relation, so although stronger or weaker feedback would effect this result, such a prescription would not at the same time also match the stellar mass relation.

3.3.1 Triaxial fit

IFU observations are limited to the inner few kpc of a galaxy and QSO absorption spectra are limited to viewing one line of sight. In light of this, it is very difficult to get any data on the general shape of the CGM out to the virial radius. To get a theoretical handle on its shape and provide some numerical estimates for further use by models, we use the inertia tensor to give a rough quantity of the shape. The inertia tensor is a 3×3 matrix, which in the common definition is the sum of tensor products of all the particle positions weighted by their masses. The eigenvectors of the inertia tensor point in the 3 orthogonal directions of the major, intermediate, and minor axes. The eigenvalues of the inertia tensor are the lengths of the major axis and two orthogonal minor axes. These eigenvalues thus define a triaxial ellipsoid.

We wish to focus our study of CGM shape on only halo gas, so we try to exclude disc gas from our shape measurement. Low density is the best determinant of halo gas, so we classify the halo as all gas with gas density, $n < 10^{-2} \text{ cm}^{-2}$, and lies outside $0.1R_{\text{vir}}$. The density was chosen as the density where self-shielding starts becoming effective. We did not add a temperature cut because some analyses of the CGM have found that it is surprisingly cold. We did not

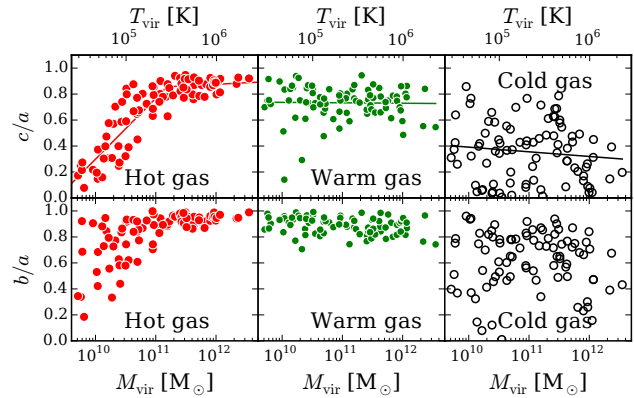


Figure 13. c/a (upper panels) and b/a (lower panels) for the gas shape (without the disc in $0.5R_{\text{vir}}$, this radius is a compromise between being too close, which would mean not capturing enough of the halo and too far, where the CGM is already so well mixed, that no structure would be recognisable.) in three temperature ranges. Hot gas: $T/K > 10^6$ (red circles), warm gas: $3 \times 10^4 < T/K < 3 \times 10^5$ (green circles) and cold gas: $T/K < 15000$ (black open circles). Lines show fits to the data in the respective color. Fit values can be seen in table 2.

want a temperature cut in our definition to preclude this possibility in our analysis.

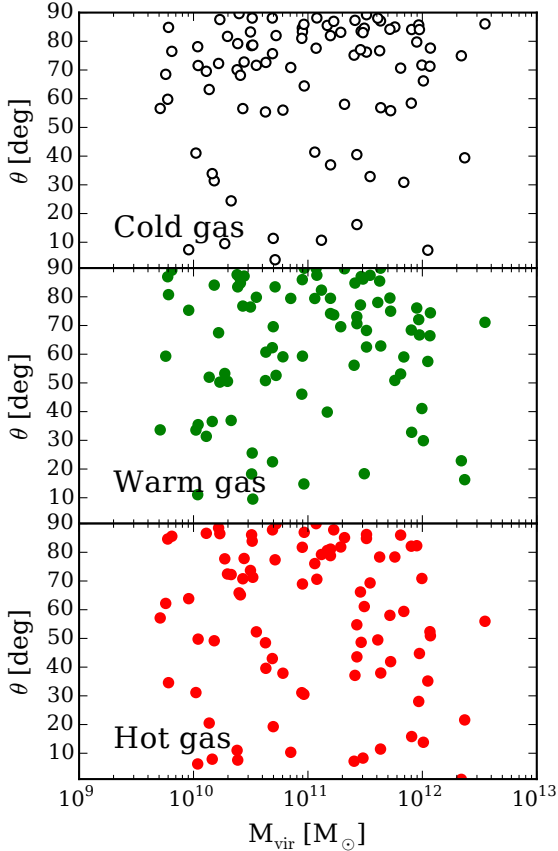
Fig. 13 shows the eigenvalues of the inertia tensor for halo inside $0.5R_{\text{vir}}$. The upper panels show c/a , where a is the major axis and c the minor axis of the fitted ellipsoid as a function of total mass of the galaxy. The lower panels show b/a , where b is the middle axis of the fit. The left panels show the hot gas (red circles, $T > 10^6$ K) in each galaxy. The right panels show the intermediate (green circles, $3 \times 10^4 < T/K < 3 \times 10^5$) and cool gas (white circles, $T < 1.5 \times 10^4$ K) for each NIHAO galaxy. The three temperature regimes are roughly the portions of the cooling curve dominated by 3 different cooling processes. The hot regime is dominated by bremsstrahlung, the warm is dominated by metal cooling, while the cool regime is dominated by hydrogen and helium line cooling. The lines represent simple fits to the distribution of c/a . The fitting parameters are given in table 2.

The c/a distribution of the hot gas rises steadily with mass up to around $2 \times 10^{11} M_{\odot}$. We present the power law fits to the c/a ratios in 2 of the appendix. Since the b/a ratio also grows with a similar, albeit not so strong trend, the hot gas distribution transforms from being prolate at low masses (small c/a and small b/a) to being mostly oblate or even spherical at high masses. The flattening at high masses can be understood with galaxy virial temperatures in mind. The virial temperature is the peak temperature inflowing gas can reach falling into a potential well. Anything higher, so for most NIHAO galaxies our hot CGM gas, should come from gas heated by stellar feedback.

For the most massive galaxies, our hot CGM threshold is their virial temperature. We expect more massive galaxies where the gas is heated by gravitational infall should be more spherical. The hot gas already attains a spherical shape in galaxies with lower virial temperature than 10^6 K. The hot CGM may become spherical at slight lower masses

Table 2. Fitting parameters for the $M_{\text{vir}}-c/a$ relation in Fig. 13. Parameters are of the form $c/a = \alpha \cdot \log_{10}(M_{\text{vir}}) + c$.

	T/K	α	c
Hot gas ($M_{\text{vir}} < 2 \times 10^{11} M_{\odot}$)	$T > 10^6$	0.469	-4.395
Hot gas ($M_{\text{vir}} > 2 \times 10^{11} M_{\odot}$)	$T > 10^6$	0.023	0.596
Warm gas	$3 \times 10^4 < T < 3 \times 10^5$	0.004	0.771
Cold gas	$T < 15000$	-0.036	0.751

**Figure 14.** Angle θ between the rotation axis of the disc and the major axis of the inertia tensor fit as a function of virial mass. 90° indicates that the major extent of the fitted gas is in the plane of the disc, while 0° indicates gas extending perpendicular to the disc. Each panel shows a different temperature range of the gas, as denoted on the plots.

(lower virial temperatures) due to winds reaching sufficient distances from the galaxy, and then being blown back and shaped by the ambient CGM.

Warm gas does not exhibit the same trend with c/a as the hot gas at low masses. Both the c/a and the b/a values stay relatively constant and high (~ 0.8) across all halo masses indicating a mostly spherical shape. The relatively high c/a and b/a values are due to the fact that this gas is both cooling out from the halo and isotropically falling inwards. Some of this is also gas that has been heated by stellar feedback and blown out perpendicular to the plane of the disc.

The cold gas exhibits the lowest c/a values, as one would

expect since it is dominated by the inner disc. One would further expect a cold gas disc to have high b/a values since those axes should be approximately the same length. For the most part, the b/a values are high in Fig. 13, though they tend towards lower values at low and high masses.

3.3.2 CGM-Disc orientation

Since outflows are expected to be aligned perpendicular to the plane of the disc, the hot CGM should appear bipolar in galaxies with lower virial temperatures than 10^6 K. The prolate shape at low masses could indicate that the hot CGM is configured as a bipolar outflow. To understand whether this is the case, we present Fig. 14. It shows the angle between the angular momentum vector of the disc and the major axis of the inertia tensor. The angle is plotted as a function of M_{vir} . A 90° angle indicates that the major moment of inertia axis lies in the plane of the disc, while 0° indicates the gas is perpendicular to the disc.

There is no trend with mass for either the hot or warm gas. In the angle analysis, the alignment appears random. Since the warm and also the hot gas is for the most part spherically shaped, it is not surprising that the orientation of the major axis of the inertia tensor is random.

At low mass, some of the random alignment may not come from the outflow but from the disc angular momentum vector. Stellar feedback drives so much turbulence that most NIHAO galaxies with $M_{\text{vir}} < 10^{11} M_{\odot}$ do not have well ordered thin discs Obreja et al. (2016), in effect making the direction given to the disc random.

The only temperature gas that does not have random scatter of angle values is the cold gas. For the cold gas, the angle clusters around 90° . Such a configuration is consistent with an extended cool gas disc.

The lack of a clear bipolar shape out to large radii is consistent with our velocity dispersion analysis which showed a fading away of the bipolarity at around 40 kpc. Even the smallest NIHAO galaxies have virial radii larger than this.

3.4 Chemical composition of the CGM with galaxy mass

Lastly, we attempt to portray the chemical makeup of the CGM and the disc separately and how these change as a function of halo mass in our simulations. We follow Suresh et al. (2015) and define the disc as all gas inside $0.1R_{\text{vir}}$ with a density higher than 0.01 cm^{-3} , and the CGM all other gas inside R_{vir} . Thus, CGM gas is characterised according to its diffuse nature, but the definition allows satellite galaxies and streams that may have pockets of higher density gas to be classified as part of the halo. In this way, the definition includes all gas inside R_{vir} .

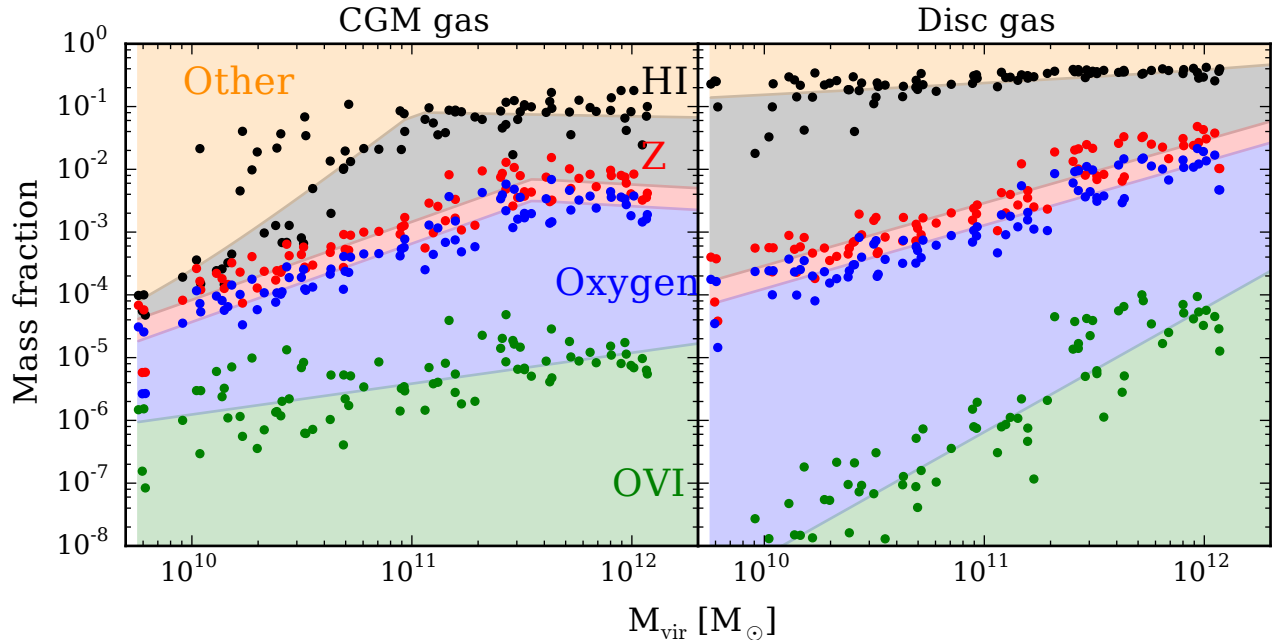


Figure 16. Mass fraction of gas split into chemical components. The plot should be read from top to bottom: Of all gas in a given halo mass range, the fraction of gas that is HI is given by the black line and the amount in metals is given by the red line. Of all metals, the mass fraction in oxygen is given by the blue line. Of all oxygen, the mass fraction in OVI is given by the red line. Each line is a fit to the data points and the fit parameters are given in table 3.

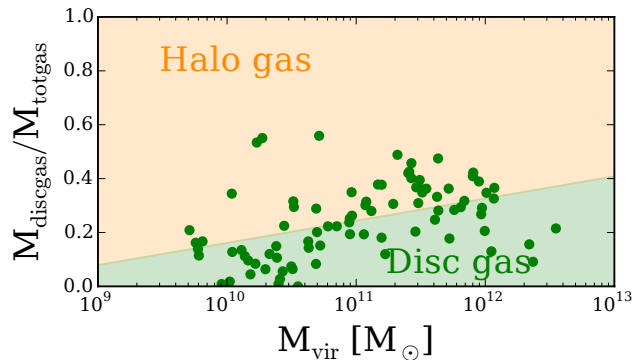


Figure 15. Mass fraction of disc gas relative to the total amount of gas. A power law fit to the data is shown as the boundary of the coloured areas. The parameters of the fit are given in table 3.

Fig. 15 shows the disc gas mass fraction of all the gas inside R_{vir} . The disc gas fractions are plotted as a function of M_{vir} . In nearly every case, the halo gas comprises the majority of the gas inside R_{vir} (note the logarithmic axes), and in some cases even more so. The disc gas fraction shows a large amount of scatter. Below $3 \times 10^{10} M_{\odot}$, the disc gas fraction varies from almost nothing to over 50%. The high variation corresponds with the bursty star formation that happens in such low mass galaxies. The high disc gas fractions represent galaxies that haven’t had much recent star formation, while the low disc gas fraction galaxies have had a starburst that blew their cool, dense disc gas away. The NIHAO sample includes few galaxies over $M > 10^{12} M_{\odot}$, but the three that show up in Fig. 15 indicate that the disc gas fraction starts

to drop above $10^{12} M_{\odot}$. The pattern is reminiscent of galaxy formation efficiency found using abundance matching techniques (Guo et al. 2010; Moster et al. 2013; Behroozi et al. 2013). One expects the disc gas mass to appear similar to star formation efficiency since stars must form out of cool, dense gas.

Fig. 16 shows the mass fractions of the cool and hot gas tracers, OVI and HI, out of the total gas masses for the halo and disc gas components separately. Since OVI is a particular ionic species of oxygen, which itself is a metal, the colored OVI and oxygen regions are subfractions of the larger region of which they are part. The region of the plot above the “Z” metals line is comprised of hydrogen and helium. The part labeled “HI” is the neutral hydrogen component. For clarity, we note that the HI line and points are the HI mass fraction added to the metals mass fraction $(M_{\text{HI}} + M_{\text{Z}})/M_{\text{tot},X}$.

The behavior of the halo and disc gas fraction differ as a function of mass. In the halo, the fractions of the species we tracked increase with increasing M_{vir} to some threshold mass at which point they flatten out and stop rising as a function of mass and may start to decline slightly. In the disc, the fractions of each component continues rising steadily through the high end of the NIHAO mass range.

The metals are all produced as the result of star formation, so one expects the metal fraction to increase in galaxies forming stars. Except for the extreme low mass end, the NIHAO galaxies form stars throughout their lifetimes. The continued increase in the disc metal gas fraction reflects the continued star formation. The halo metals gas fraction flattens because metal enriched outflows decrease significantly, or stop altogether, once galaxies surpass some mass threshold as it becomes harder for winds to escape the disc in the more massive gravitational potential wells (see Muratov

Table 3. Fitting parameters for the power law fits in fig. 16. Parameters are of the form $\log_{10}(f_X) = \alpha \cdot \log_{10}(M_{\text{vir}}) + c$.

	Name	M_{vir} range	α	c
Halo gas	HI	$< 1 \times 10^{11} M_{\odot}$	2.643	-30.202
	HI	$> 1 \times 10^{11} M_{\odot}$	-0.050	-0.589
	Z	$< 5 \times 10^{11} M_{\odot}$	1.214	-16.208
	Z	$> 5 \times 10^{11} M_{\odot}$	-0.309	1.476
	O	$< 5 \times 10^{11} M_{\odot}$	1.219	-16.608
	O	$> 5 \times 10^{11} M_{\odot}$	-0.315	1.202
Disc gas	OVI	all	0.492	-10.823
	HI	all	0.183	-2.643
	Z	all	1.00	-13.534
	O	all	1.011	-14.013
Disc/Total	OVI	all	1.972	-27.880
		all	0.082	-0.662

et al. 2015, for a detailed study of this). Based on this, the threshold halo mass at which the flattening occurs is a tug-of-war point between feedback strength, which pushes gas outward, and the depth of the gravitational well. As such, if this turnover mass were measured observationally, it could set a constraint for the strength of feedback models.

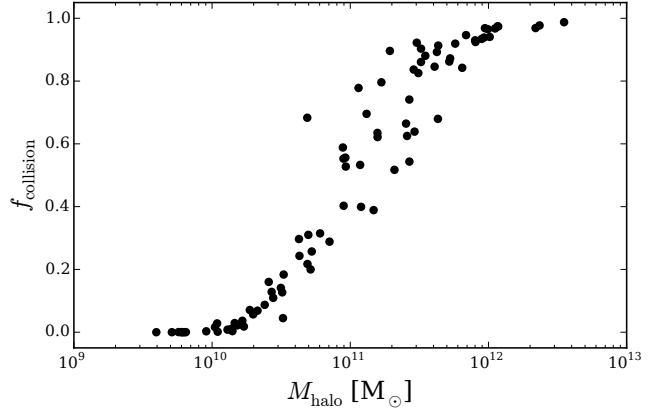
The metals reach the mass threshold where their mass fractions flatten around $3 \times 10^{11} M_{\odot}$. HI flattens at a lower mass around $M_{\text{vir}} = 10^{11} M_{\odot}$. Different physics governs the HI fraction, since it does not increase due to star formation. Its fraction is dominated by ionization; “other” gas in the halo is mostly ionized hydrogen. Whether the HI fraction comes from outflows or is simply a natural consequence of the gas density profiles of galaxies is a question for study in future work. The sharp decrease in HI fraction in some of the lower mass galaxies reflects the lack of any dense gas in the halos of those galaxies.

The OVI trend is ambiguous as it has the largest scatter of any species, so if the high boundary is indicative of the OVI fraction, then the OVI fractions reduces. The OVI can also be well fit using a single power law, which we have done for simplicity. OVI is a similar case to HI since it will depend on the ionization conditions. The virial temperature of the most massive halos is around the ionisation temperature for OVI.

While it is hard to see on the logarithmic scale, the disc HI fraction grows by a factor of a few over the halo mass range. That trend follows the disc gas mass fraction, and reflects the increasing gas densities with M_{vir} .

The OVI fraction in the disc increases the most steeply of any species, with a slope $M_{\text{disc, OVI}} \propto M_{\text{vir}}^2$. That increase reflects the deeper disc potential, which is able to hold onto more hot gas as the galaxy gets more massive.

To each mass fraction, we fit power laws. In the case of the gas in the halo, we fit a broken power law to the HI, the metallicity and the oxygen components. The threshold for the break was chosen “by eye” and is $10^{11} M_{\odot}$ for HI and $5 \times 10^{11} M_{\odot}$ for both the metallicity and the oxygen components. The fitting parameters are given in table 3.

**Figure 17.** Mass fraction of OVI in the CGM created by collisional ionisation per galaxy as a function of halo mass. OVI in low mass galaxies is mainly created through photoionisation from the UV background. Massive galaxies have a large fraction of OVI that is collisionally ionised.

4 DISCUSSION

In general, the simulated CGM compares well with current observations, but two problems stand out: 1) the OVI simulated column densities are almost 1 dex lower than observations; and 2) optically thick HI extends much further in observations than simulations.

4.1 OVI deficit

We use the suite of 86 NIHAO simulations to analyse the CGM and the extent of OVI column densities out past the virial radius of galaxies from $\log(M_{\text{halo}}/M_{\odot}) \sim 9 - 12$. The right panel of Fig. 3 shows how the predicted OVI column density changes with the stellar mass of the galaxy. Fig. 4 shows the changes with impact parameter and luminosity and includes the observations. We underpredict OVI at all radii and for all galaxy luminosities by about the same amount everywhere, approximately 1 dex. The origin of this discrepancy is not yet well understood, but has been seen in most galaxy formation simulations to date (Hummels et al. 2013; Suresh et al. 2015; Ford et al. 2015). While Suresh et al. (2015) suggest that the observations are consistent with a constant column density across galaxy mass/luminosity, the observations are also consistent with an increase to around $1L^*$, above which the trend flattens off. In the simulations, the plateau is at $\log(N_{\text{OVI}}/\text{cm}^{-2}) \sim 13.5$ in each radial range. The plateau is reached at progressively higher luminosities at larger radii.

The observational data is relatively sparse and shows a fairly broad scatter, but there may be a similar plateau that is higher than the simulations, at $\log(N_{\text{OVI}}/\text{cm}^{-2}) \sim 14$.

OVI can be photoionised at low temperatures and low densities ($T \lesssim 10^{4.5} \text{ K}$, $\rho \lesssim 10^{-4} \text{ cm}^{-3}$) by incoming radiation assuming photoionisation equilibrium (see Kollmeier et al. 2014, for possible shortcomings of this assumption) and a constant UV background. Assuming collisional ionisation equilibrium produces OVI in denser gas ($\rho \gtrsim 10^{-4} \text{ cm}^{-3}$) with temperatures around $10^5 - 10^6 \text{ K}$. Disentangling these two channels is vital to get the correct amount of OVI.

Fig. 17 shows the mass fraction of OVI in the CGM produced by collisional ionisation, $f_{\text{collision}}$, as a function of halo mass for all NIHAO galaxies. The definition of CGM is the same as in the rest of the paper and $f_{\text{collision}}$ is defined as the fraction of OVI above 10^5 K with respect to the total amount of OVI in the CGM per galaxy. This approximation of the amount of collisionally ionised OVI is adequate to get a sense of the trend as a function of halo mass, which is all we are interested in here.

Small galaxies are mainly photoionised, while massive galaxies are predominantly collisionally ionised. The approximate threshold halo mass between these two regimes is $10^{11} M_{\odot}$. This is caused by the fact that much of the CGM gas is around the virial temperature, which enters the OVI collisional ionisation regime at about this halo mass, being too low for smaller galaxies.

The assumption of collisional ionisation equilibrium (CIE) generally works best in high density, low temperature regions. Not assuming CIE has been tested in a variety of non-equilibrium models (see Cen & Fang 2006; Savage et al. 2014; Oppenheimer et al. 2016). Cen & Fang (2006) show a decrease in the OVI column densities relative to CIE since the shock heated gas is initially above 10^6 K and cools through the collisional ionisation regime. Conversely, (Savage et al. 2014) show that non-CIE models can increase the amount of OVI produced through collisional ionisation at temperatures below 10^5 K. Although testing non-CIE models might hold the answer to the OVI deficit, it is beyond the scope of this paper.

Ford et al. (2015) point out that while the virial temperature of massive halos around $10^{12} M_{\odot}$ is around 10^6 K, most gas that is photoionized into the OVI state has a temperature around $10^{4.5}$ K. OVI ionisation might best be explained as a transient state of hot gas cooling out of the halo. Simulations have a hard time capturing non-equilibrium states, so they might therefore show a persistent deficit in OVI. Rahmati et al. (2015) find that collisional ionisation is a non-negligible effect for OVI. Collisional ionisation fractions are above 20% for $z = 0.1$ in their fiducial model.

The only way photoionisation from the UV background could be the dominant process in producing OVI in massive halos above $10^{11} M_{\odot}$ would be if the CGM gas were systematically cooler. This means either the gas never shock heated to the virial temperature or the cooling time is short enough to pass through the collisional ionisation range without exciting OVI. But since simulations generally have trouble with the overproduction of stars, a further enhanced cooling time would worsen this problem.

Both Shen et al. (2012) and Suresh et al. (2015) ran models that included local sources of photoionisation to test whether this significantly effects the overall amount of OVI. Both found that the effect is negligible for $r \gtrsim 50$ kpc. So, although this could ameliorate the OVI deficit in the center of haloes, this is not sufficient to account of the large amounts at larger radii.

The two main pieces of physics that contribute to the OVI column density are *stellar feedback* that drives galactic outflows and the *radiation field*. The detailed interaction of stellar feedback with the interstellar medium and the CGM are poorly resolved in simulations. The shock fronts occur on small scales relative to the distance that the outflowing gas travels, so they are difficult to model. In spite of the

poor resolution, S12 and Hummels et al. (2013) showed the strength of stellar feedback has a big impact on OVI column densities. Also, if resolution was a major cause of error, the NIHAO simulations would show a clear difference in CGM properties with halo mass, since the physical resolution decreases with increasing galaxy mass.

Fig. 16 shows that there is plenty of oxygen in the CGM, so matching the observations seems not to be a matter of transport, but one of getting it into the correct ionization state. Hummels et al. (2013) tested manually varying either the density, the metallicity or the temperature of their simulations. Only the simulations with feedback and outflows and a manually decreased temperature (to 3×10^5 K) could produce enough OVI to reproduce the observations. They note that temperature structure of the CGM is dependent on resolution within $r \gtrsim 50$ kpc based on their thermal feedback prescription.

An intrinsic error in our method to be noted is that we only account for gas absorption within ~ 4 Mpc of the galaxies. We are aware that quasar sightlines pass through a larger volume, possibly gathering additional absorption lines along this path. This would cause our column densities to be underestimated. We assume this effect to be small, similar to other analysis such as Hummels et al. (2013).

4.2 Extended HI

One of the more mysterious discoveries about the CGM has been observations of optically thick, cool, neutral gas covering large cross sections surrounding galaxies (Hennawi et al. 2006; Prochaska et al. 2013; Werk et al. 2014). Particularly perplexing is that the cool gas covering fractions increase when looking at more massive galaxies that are also quasars (Prochaska et al. 2014). Naively, more massive galaxies should have hotter CGMs and quasars should ionize any neutral gas. Observations show the opposite: quasars have more cool, neutral gas in the form of small, dense clouds.

Our simulations are not ideally suited to study the CGM of massive galaxies at high z ; NIHAO is focused on galaxies smaller than the Milky Way at $z = 0$. However, we present a comparison to give some idea of how our simulations perform on this problem. Our HI ionisation fraction takes self-shielding into account, which has the effect of increasing the amount of HI in high density regions. Fig. 7 shows that optically thick HI covers a small fraction of R_{vir} at $z = 0$, but that the NIHAO simulations cover a large fraction at higher redshift that approaches the observed value. While the fraction of R_{vir} covered increases with redshift, Fig. 7 also shows that the physical area covered changes little.

Fig. 9 shows that the simulations match the cool gas column densities very well in the inner regions of the CGM. The simulations have trouble producing high enough HI column densities in the CGM outskirts.

This is a general discrepancy between observations and simulations that has not been solved: why there is so much cool gas at such large distances from galaxies? In an evolving galaxy there are two possibilities: cool gas clouds are ejecta from the disc or gas cools at large distances and is in the early stages of accreting onto the galaxy.

Since the cool gas is not pressure supported, cooling

condensations contribute to overcooling in simulations as the clouds fall onto the disc. It remains a mystery how clouds like those observed continue to be supported at large distances in the CGM, since they do not appear to contribute to star formation.

SPH simulations without a careful numerical treatment of hydrodynamics will overestimate these cooling condensations (Maller & Bullock 2004). Such condensations are the numerical embodiment of the Field (1965) instability. Agertz et al. (2007) identified such blobs as a numerical problem in SPH that does not exist in grid simulations, where cool clouds are quickly destroyed when moving through a hot medium.

Hints to solve the mystery are coming from focused, high resolution simulations. Quataert et al. (2015) showed that magnetic fields can provide internal pressure for cool clouds and allow those cool clouds to survive for much longer times. High resolution simulations are also being used to understand how cool gas can be driven out of galaxies. Scannapieco & Brügger (2015) simulated cold gas clouds in supersonic flows and found that they survived longer than clouds in subsonic flows because the shock front suppresses the Kelvin-Helmholtz instability. Such enhancements allow cold clouds to survive out to several kiloparsec from galaxies, but not hundreds of kiloparsec where HI is observed.

Brügger & Scannapieco (2016) adds thermal electrons to the Scannapieco & Brügger (2015) simulations. Conduction efficiently heats the cloud below a threshold density. When the cloud is more dense, it collapses into a dense filament that is able to radiate away any energy that conducts into its center, which also lengthens its lifetime. Adding to prior research, Thompson et al. (2015) take into account the rapid destruction of cool clouds entrained in a hot $\sim 10^7$ K outflow. They suggest that the cool gas in the CGM outskirts has two sources. An initial source is hot outflowing gas that radiatively cools. A secondary source is the gas that cools out of the shock front created as the wind plows into the CGM.

These modelers suggest that galactic winds include physics that is too difficult for simulations to model and provide prescriptions to include the physics in simulations. It is unclear whether it is possible to easily include such prescriptions. Faucher-Giguère et al. (2015) has shown promising results in fully self-consistent simulations using higher resolution. For instance, higher resolution adds a significant area of optically thick gas. Rahmati et al. (2015) were also able to match the HI column densities even at large distances from the galaxy using strong stellar and AGN feedback. Combining insights from both high resolution models and more advanced simulations can help to deepen our understanding of how the CGM is created and evolves.

5 SUMMARY

We analysed the CGM of the NIHAO galaxy simulation suite, which includes 86 galaxies ranging in halo mass from $10^{9.7} - 10^{12.5} M_{\odot}$. The galaxies follow the stellar mass–halo mass relation (Wang et al. 2015) and the disc gas–stellar mass relation (Stinson et al. 2015).

The hot and cold gas phases were examined using the commonly observed OVI and HI ions. We compared their

column density profiles with observations, studied the covering fractions of dense HI, looked at the shape of the CGM and studied its chemical composition. Our goal was to present the simulations so that observers and modellers can compare with them in future studies.

We combined column densities of HI and OVI from all of the galaxies in NIHAO according to both the luminosity of the galaxy and impact parameter of the measured column density. Overall, the simulations provide a good match to observations. The column density of OVI increases as a function of galaxy luminosity to a plateau. Observations are still too sparse to make definite conclusions, but the simulations seem to follow the same functional form. Using an updated self-shielding approximation (Rahmati et al. 2013), the simulated HI column densities follow observations more closely than OVI. At $z = 3$, optically thick HI covers the same fraction of R_{vir} as the observations.

In addition to the successes of the simulations, two problems common to many numerical simulations are apparent. While the trend of the OVI simulations with luminosity agrees with observations, its normalization is about 0.7 dex too low, a trend commonly seen in simulations (e.g. Hummels et al. 2013; Ford et al. 2015; Suresh et al. 2015). In S12, this discrepancy was not as apparent, since they examined just two galaxies and used a slightly stronger feedback model than what was used in NIHAO. We do not propose using stronger feedback to create more OVI because it would reduce star formation too much. Instead, we point to the large amount of oxygen present in the CGM and conclude that our OVI ionization fraction is incorrect, possibly due to the temperature structure of the CGM.

Second, the extent of optically thick HI ($\log N_{\text{HI}} > 17.2$) covers too small a fraction of the projected area, particularly between R_{vir} and $2R_{\text{vir}}$. The source of the large amount of cool gas observed in the outer CGM and how it stays out there remains unknown. Unfortunately, our simulations shed little new light on the mystery. We simply note that that optically thick HI covers the same physical area as a function of galaxy halo mass at all redshifts in the simulations.

Given the similarity of the simulations and observations, we extend our analysis to the outflows that transport gas and metal enrichment to the CGM. Specifically, we recreate observations of gas velocity dispersion around edge-on discs. Wild et al. (2014) proposed that heightened velocity dispersions perpendicular to the disc with respect to the velocity dispersion in the disc plane are evidence for bipolar outflows. We detect a signal in intermediate mass galaxies ($10 \lesssim \log M_{\text{Halo}}/M_{\odot} \lesssim 11.5$), though the ratio never exceeds two. Such enhanced velocity dispersions are visible in maps out to around 40 kpc in this halo mass range. 40 kpc is the same distance to which Bordoloi et al. (2014) observes outflows. Beyond 40 kpc, the velocity dispersion signal is isotropic. Larger halos do not show this signal, since their inner CGM is dominated by an extended gas disc which lies in the plane of the stellar disc.

Given the weak outflow signal, it is perhaps no surprise that it is hard to find any evidence for bipolar shapes in our simulations. Using the inertia tensor, we studied the shape distribution for three different gas temperatures. The hot ($T > 10^6$ K) gas showed a somewhat bipolar shape in the lowest mass simulations. The direction of the long

axis was uncorrelated with the disc angular momentum axis. So, at $z = 0$, bipolar outflows do not make up a dominant mass component of the CGM. Rather, the CGM shape is mostly spherical because of virialization and the interaction of outflows with the ambient CGM. The cool ($T < 10^4$ K) CGM is an extended disc, while warm gas ($3 \times 10^4 < T/K < 3 \times 10^5$) is always spherical.

The chemical enrichment of both the disc and the halo follow expected monotonically increasing trends. The mass fractions of HI, metals, oxygen and OVI can be well fit with power laws as a function of halo mass. The power law fits might be useful in galaxy formation models that do not use full hydrodynamics, such as semi-analytical models. Most notably, there is much more oxygen than what is shown as OVI, so fixing the OVI problem is not a transport problem, but an ionisation problem.

Our analysis here focused on the $z = 0$ universe. More work is necessary to put these results into context of the high redshift universe.

ACKNOWLEDGMENTS

We thank the anonymous referee for a helpful report. We also thank Aura Obreja, Tobias Buck, Jonathan Stern, Joe Hennawi, and Glenn van de Ven for helpful suggestions and useful conversations.

The NIHAO simulations were run using the galaxy formation code GASOLINE, developed and written by Tom Quinn and James Wadsley. Without their contributions, this paper would have been impossible.

TAG, GSS and AVM acknowledge funding by Sonderforschungsbereich SFB 881 “The Milky Way System” (subproject A1) of the German Research Foundation (DFG).

The analysis was performed using the pynbody package (<http://pynbody.github.io/>, Pontzen et al. 2013), written by Andrew Pontzen and Rok Roškar in addition to the authors.

The simulations were performed on the THEO cluster of the Max-Planck-Institut für Astronomie, the HYDRA cluster at the Rechenzentrum in Garching, and the MILKY WAY supercomputer, funded by the Deutsche Forschungsgemeinschaft (DFG) through the Collaborative Research Center (SFB 881) “The Milky Way System” (subproject Z2), hosted and co-funded by the Jülich Supercomputing Center (JSC).

REFERENCES

- Agertz O., Moore B., Stadel J., Potter D., Miniati F., Read J., Mayer L., Gawryszczak A., Kravtsov A., Nordlund Å., Pearce F., Quilis V., Rudd D., Springel V., Stone J., Tasker E., Teyssier R., Wadsley J., Walder R., 2007, *MNRAS*, 380, 963
- Aguirre A., Hernquist L., Schaye J., Katz N., Weinberg D. H., Gardner J., 2001, *ApJ*, 561, 521
- Aumer M., White S. D. M., Naab T., Scannapieco C., 2013, *MNRAS*, 434, 3142
- Behroozi P. S., Wechsler R. H., Conroy C., 2013, *ApJ*, 770, 57
- Birnboim Y., Dekel A., 2003, *MNRAS*, 345, 349
- Bordoloi R., Lilly S. J., Hardmeier E., Contini T., Kneib J.-P., Le Fevre O., Mainieri V., Renzini A., Scodreggio M., Zamorani G., Bardelli S., Bolzonella M., Bongiorno A., Caputi K., Carollo C. M., Cucciati O., de la Torre S., de Ravel L., Garilli B., Iovino A., Kampeczyk P., Kovač K., Knobel C., Lamareille F., Le Borgne J.-F., Le Brun V., Maier C., Mignoli M., Oesch P., Pello R., Peng Y., Perez Montero E., Presotto V., Silverman J., Tanaka M., Tasca L., Tresse L., Vergani D., Zucca E., Cappi A., Cimatti A., Coppa G., Franzetti P., Koekemoer A., Moresco M., Nair P., Pozzetti L., 2014, *ApJ*, 794, 130
- Brüggen M., Scannapieco E., 2016, *ArXiv e-prints* 1602.01843
- Cen R., Chisari N. E., 2011, *ApJ*, 731, 11
- Cen R., Fang T., 2006, *ApJ*, 650, 573
- Christensen C. R., Davé R., Governato F., Pontzen A., Brooks A., Munshi F., Quinn T., Wadsley J., 2015, *ArXiv e-prints* 1508.00007
- Cowie L. L., Songaila A., 1995, *ApJ*, 453, 596
- Crain R. A., McCarthy I. G., Frenk C. S., Theuns T., Schaye J., 2010, *MNRAS*, 407, 1403
- Crighton N. H. M., Hennawi J. F., Prochaska J. X., 2013, *ApJ*, 776, L18
- Crighton N. H. M., Hennawi J. F., Simcoe R. A., Cooksey K. L., Murphy M. T., Fumagalli M., Prochaska J. X., Shanks T., 2015, *MNRAS*, 446, 18
- Dalla Vecchia C., Schaye J., 2008, *MNRAS*, 387, 1431
- , 2012, *MNRAS*, 426, 140
- Danforth C. W., Keeney B. A., Tilton E. M., Shull J. M., Stevans M., Pieri M. M., Stocke J. T., Savage B. D., France K., Syphers D., Smith B. D., Green J. C., Froning C., Penton S. V., Osterman S. N., 2014, *ArXiv e-prints* 1402.2655
- Davé R., Finlator K., Oppenheimer B. D., 2011, *MNRAS*, 416, 1354
- Davé R., Oppenheimer B. D., 2007, *MNRAS*, 374, 427
- Dehnen W., Aly H., 2012, *MNRAS*, 425, 1068
- Di Cintio A., Brook C. B., Macciò A. V., Stinson G. S., Knebe A., Dutton A. A., Wadsley J., 2014, *MNRAS*, 437, 415
- Durier F., Dalla Vecchia C., 2012, *MNRAS*, 419, 465
- Dutton A. A., Macciò A. V., 2014, *MNRAS*, 441, 3359
- Faucher-Giguere C.-A., Feldmann R., Quataert E., Keres D., Hopkins P. F., Murray N., 2016, *ArXiv e-prints* 1601.07188
- Faucher-Giguere C.-A., Hopkins P. F., Kereš D., Muratov A. L., Quataert E., Murray N., 2015, *MNRAS*, 449, 987
- Ferland G. J., Korista K. T., Verner D. A., Ferguson J. W., Kingdon J. B., Verner E. M., 1998, *PASP*, 110, 761
- Field G. B., 1965, *ApJ*, 142, 531
- Ford A. B., Werk J. K., Dave R., Tumlinson J., Bordoloi R., Katz N., Kollmeier J. A., Oppenheimer B. D., Peebles M. S., Prochaska J. X., Weinberg D. H., 2015, *ArXiv e-prints* 1503.02084
- Fumagalli M., Hennawi J. F., Prochaska J. X., Kasen D., Dekel A., Ceverino D., Primack J., 2014, *ApJ*, 780, 74
- Girardi L., Williams B. F., Gilbert K. M., Rosenfield P., Dalcanton J. J., Marigo P., Boyer M. L., Dolphin A., Weisz D. R., Melbourne J., Olsen K. A. G., Seth A. C., Skillman E., 2010, *ApJ*, 724, 1030
- Guo Q., White S., Li C., Boylan-Kolchin M., 2010, *MNRAS*, 404, 1111
- Haardt F., Madau P., 2001, in *Clusters of Galaxies and the High Redshift Universe Observed in X-rays*, Neumann

- D. M., Tran J. T. V., eds.
—, 2005, unpublished
- Hayward C. C., Hopkins P. F., 2015, ArXiv e-prints
- Hennawi J. F., Prochaska J. X., Burles S., Strauss M. A., Richards G. T., Schlegel D. J., Fan X., Schneider D. P., Zakamska N. L., Oguri M., Gunn J. E., Lupton R. H., Brinkmann J., 2006, *ApJ*, 651, 61
- Hopkins P. F., Kereš D., Oñorbe J., Faucher-Giguère C.-A., Quataert E., Murray N., Bullock J. S., 2014, *MNRAS*, 445, 581
- Hopkins P. F., Quataert E., Murray N., 2012, *MNRAS*, 421, 3522
- Hummels C. B., Bryan G. L., Smith B. D., Turk M. J., 2013, *MNRAS*, 430, 1548
- Kacprzak G. G., Muzahid S., Churchill C. W., Nielsen N. M., Charlton J. C., 2015, *ApJ*, 815, 22
- Kannan R., Stinson G. S., Macciò A. V., Hennawi J. F., Woods R., Wadsley J., Shen S., Robitaille T., Cantalupo S., Quinn T. R., Christensen C., 2014, *MNRAS*, 437, 2882
- Keller B. W., Wadsley J., Benincasa S. M., Couchman H. M. P., 2014, *MNRAS*, 442, 3013
- Kereš D., Katz N., Weinberg D. H., Davé R., 2005, *MNRAS*, 363, 2
- Kollmeier J. A., Weinberg D. H., Oppenheimer B. D., Haardt F., Katz N., Davé R., Fardal M., Madau P., Danforth C., Ford A. B., Peebles M. S., McEwen J., 2014, *ApJ*, 789, L32
- Lehner N., O’Meara J. M., Fox A. J., Howk J. C., Prochaska J. X., Burns V., Armstrong A. A., 2014, *ApJ*, 788, 119
- Maller A. H., Bullock J. S., 2004, *MNRAS*, 355, 694
- Marigo P., Girardi L., Bressan A., Groenewegen M. A. T., Silva L., Granato G. L., 2008, *A&A*, 482, 883
- Martin C. L., Shapley A. E., Coil A. L., Kornei K. A., Bundy K., Weiner B. J., Noeske K. G., Schiminovich D., 2012, *ApJ*, 760, 127
- Moster B. P., Naab T., White S. D. M., 2013, *MNRAS*, 428, 3121
- Muratov A. L., Kereš D., Faucher-Giguère C.-A., Hopkins P. F., Quataert E., Murray N., 2015, *MNRAS*, 454, 2691
- Murray N., Quataert E., Thompson T. A., 2005, *ApJ*, 618, 569
- Obreja A. C., Stinson G. S., Dutton A. A., Macciò A. V., Wang L., Kang X., 2016, *MNRAS*, submitted
- Oppenheimer B. D., Crain R. A., Schaye J., Rahmati A., Richings A. J., Trayford J. W., Tumlinson J., Bower R. G., Schaller M., Theuns T., 2016, *MNRAS*, 460, 2157
- Oppenheimer B. D., Davé R., 2006, *MNRAS*, 373, 1265
- Oppenheimer B. D., Davé R., Katz N., Kollmeier J. A., Weinberg D. H., 2012, *MNRAS*, 420, 829
- Oppenheimer B. D., Davé R., Kereš D., Fardal M., Katz N., Kollmeier J. A., Weinberg D. H., 2010, *MNRAS*, 406, 2325
- Pawlik A. H., Schaye J., 2008, *MNRAS*, 389, 651
- , 2011, *MNRAS*, 412, 1943
- Peebles M. S., Werk J. K., Tumlinson J., Oppenheimer B. D., Prochaska J. X., Katz N., Weinberg D. H., 2014, *ApJ*, 786, 54
- Planck Collaboration, Ade P. A. R., Aghanim N., Armitage-Caplan C., Arnaud M., Ashdown M., Atrio-Barandela F., Aumont J., Baccigalupi C., Banday A. J., et al., 2014, *A&A*, 571, A16
- Pontzen A., Roškar R., Stinson G., Woods R., 2013, *pynbody: N-Body/SPH analysis for python*. Astrophysics Source Code Library
- Price D. J., 2008, *Journal of Computational Physics*, 227, 10040
- Prochaska J. X., Hennawi J. F., Simcoe R. A., 2013, *ApJ*, 762, L19
- Prochaska J. X., Lau M. W., Hennawi J. F., 2014, *ApJ*, 796, 140
- Prochaska J. X., Weiner B., Chen H.-W., Mulchaey J., Cooksey K., 2011, *ApJ*, 740, 91
- Puchwein E., Springel V., 2013, *MNRAS*, 428, 2966
- Quataert E., Heinemann T., Spitkovsky A., 2015, *MNRAS*, 447, 3328
- Rahmati A., Schaye J., Bower R. G., Crain R. A., Furlong M., Schaller M., Theuns T., 2015, *MNRAS*, 452, 2034
- Rahmati A., Schaye J., Crain R. A., Oppenheimer B. D., Schaller M., Theuns T., 2016, *MNRAS*, 459, 310
- Rahmati A., Schaye J., Pawlik A. H., Raičević M., 2013, *MNRAS*, 431, 2261
- Rees M. J., Ostriker J. P., 1977, *MNRAS*, 179, 541
- Ritchie B. W., Thomas P. A., 2001, *MNRAS*, 323, 743
- Rudie G. C., Steidel C. C., Shapley A. E., Pettini M., 2013, *ApJ*, 769, 146
- Rudie G. C., Steidel C. C., Trainor R. F., Rakic O., Bogosavljević M., Pettini M., Reddy N., Shapley A. E., Erb D. K., Law D. R., 2012, *ApJ*, 750, 67
- Saitoh T. R., Makino J., 2009, *ApJ*, 697, L99
- Savage B. D., Kim T.-S., Wakker B. P., Keeney B., Shull J. M., Stocke J. T., Green J. C., 2014, *ApJS*, 212, 8
- Scannapieco E., Brüggem M., 2015, *ApJ*, 805, 158
- Schaye J., Aguirre A., Kim T.-S., Theuns T., Rauch M., Sargent W. L. W., 2003, *ApJ*, 596, 768
- Schaye J., Crain R. A., Bower R. G., Furlong M., Schaller M., Theuns T., Dalla Vecchia C., Frenk C. S., McCarthy I. G., Helly J. C., Jenkins A., Rosas-Guevara Y. M., White S. D. M., Baes M., Booth C. M., Camps P., Navarro J. F., Qu Y., Rahmati A., Sawala T., Thomas P. A., Trayford J., 2015, *MNRAS*, 446, 521
- Schaye J., Dalla Vecchia C., Booth C. M., Wiersma R. P. C., Theuns T., Haas M. R., Bertone S., Duffy A. R., McCarthy I. G., van de Voort F., 2010, *MNRAS*, 402, 1536
- Shen S., Madau P., Aguirre A., Guedes J., Mayer L., Wadsley J., 2012, *ApJ*, 760, 50
- Shen S., Wadsley J., Stinson G., 2010, *MNRAS*, 407, 1581
- Springel V., Hernquist L., 2003, *MNRAS*, 339, 312
- Steidel C. C., Erb D. K., Shapley A. E., Pettini M., Reddy N., Bogosavljević M., Rudie G. C., Rakic O., 2010, *ApJ*, 717, 289
- Stinson G., Seth A., Katz N., Wadsley J., Governato F., Quinn T., 2006, *MNRAS*, 373, 1074
- Stinson G. S., Brook C., Macciò A. V., Wadsley J., Quinn T. R., Couchman H. M. P., 2013, *MNRAS*, 428, 129
- Stinson G. S., Brook C., Prochaska J. X., Hennawi J., Shen S., Wadsley J., Pontzen A., Couchman H. M. P., Quinn T., Macciò A. V., Gibson B. K., 2012, *MNRAS*, 425, 1270
- Stinson G. S., Dutton A. A., Wang L., Macciò A. V., Herpich J., Bradford J. D., Quinn T. R., Wadsley J., Keller B., 2015, *MNRAS*, 454, 1105
- Suresh J., Rubin K. H. R., Kannan R., Werk J. K., Hernquist L., Vogelsberger M., 2015, ArXiv e-prints

- 1511.00687
 Theuns T., Viel M., Kay S., Schaye J., Carswell R. F., Tzanavaris P., 2002, *ApJ*, 578, L5
 Thom C., Chen H.-W., 2008, *ApJ*, 683, 22
 Thompson T. A., Fabian A. C., Quataert E., Murray N., 2015, *MNRAS*, 449, 147
 Tollet E., Macciò A. V., Dutton A. A., Stinson G. S., Wang L., Penzo C., Gutcke T. A., Buck T., Kang X., Brook C., Di Cintio A., Keller B. W., Wadsley J., 2016, *MNRAS*, 456, 3542
 Tripp T. M., Sembach K. R., Bowen D. V., Savage B. D., Jenkins E. B., Lehner N., Richter P., 2008, *ApJS*, 177, 39
 Tumlinson J., Thom C., Werk J. K., Prochaska J. X., Tripp T. M., Katz N., Davé R., Oppenheimer B. D., Meiring J. D., Ford A. B., O’Meara J. M., Peeples M. S., Sembach K. R., Weinberg D. H., 2013, *ApJ*, 777, 59
 Tumlinson J., Thom C., Werk J. K., Prochaska J. X., Tripp T. M., Weinberg D. H., Peeples M. S., O’Meara J. M., Oppenheimer B. D., Meiring J. D., Katz N. S., Davé R., Ford A. B., Sembach K. R., 2011, *Science*, 334, 948
 Vogelsberger M., Genel S., Sijacki D., Torrey P., Springel V., Hernquist L., 2013, *MNRAS*, 436, 3031
 Vogelsberger M., Genel S., Springel V., Torrey P., Sijacki D., Xu D., Snyder G., Nelson D., Hernquist L., 2014, *MNRAS*, 444, 1518
 Wadsley J. W., Stadel J., Quinn T., 2004, *New Astronomy*, 9, 137
 Wadsley J. W., Veeravalli G., Couchman H. M. P., 2008, *MNRAS*, 387, 427
 Wang L., Dutton A. A., Stinson G. S., Macciò A. V., Penzo C., Kang X., Keller B. W., Wadsley J., 2015, *MNRAS*, 454, 83
 Werk J. K., Prochaska J. X., Tumlinson J., Peeples M. S., Tripp T. M., Fox A. J., Lehner N., Thom C., O’Meara J. M., Ford A. B., Bordoloi R., Katz N., Tejos N., Oppenheimer B. D., Davé R., Weinberg D. H., 2014, *ApJ*, 792, 8
 White S. D. M., Frenk C. S., 1991, *ApJ*, 379, 52
 White S. D. M., Rees M. J., 1978, *MNRAS*, 183, 341
 Wild V., Rosales-Ortega F., Falcón-Barroso J., García-Benito R., Gallazzi A., González Delgado R. M., Bekeraité S., Pasquali A., Johansson P. H., García Lorenzo B., van de Ven G., Pawlik M., Pérez E., Monreal-Ibero A., Lyubenova M., Cid Fernandes R., Méndez-Abreu J., Barrera-Ballesteros J., Kehrig C., Iglesias-Páramo J., Bomans D. J., Márquez I., Johnson B. D., Kennicutt R. C., Husemann B., Mast D., Sánchez S. F., Walcher C. J., Alves J., Aguerri A. L., Alonso Herrero A., Bland-Hawthorn J., Catalán-Torrecilla C., Florido E., Gomes J. M., Jahnke K., López-Sánchez Á. R., de Lorenzo-Cáceres A., Marino R. A., Mármol-Queraltó E., Olden P., del Olmo A., Papaderos P., Quirrenbach A., Vílchez J. M., Ziegler B., 2014, *A&A*, 567, A132

This paper has been typeset from a $\text{\TeX}/\text{\LaTeX}$ file prepared by the author.

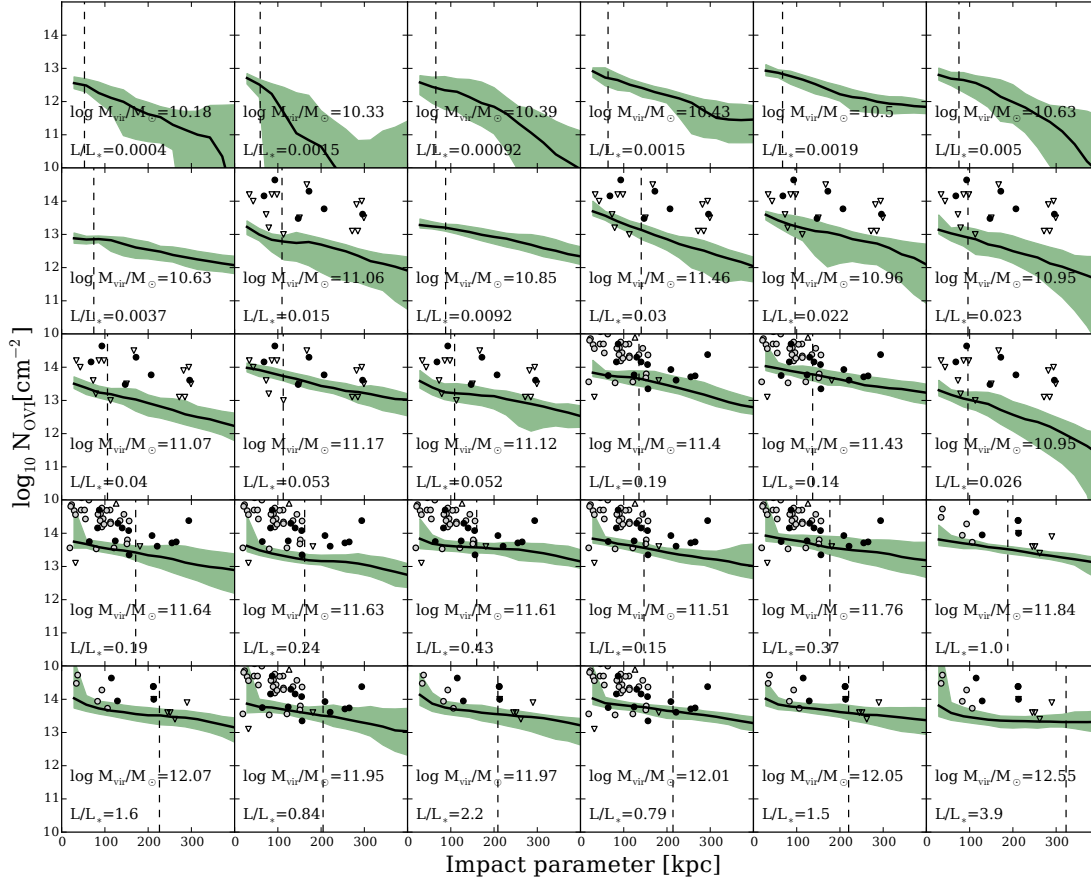


Figure A1. Mock sightline distributions of OVI column density for the same 30 NIHAO galaxies as in fig. 2 and fig. 3 and 4 of Wang et al. (2015). Black solid lines indicate the median column density for a given impact parameter bin. The green-gray shaded area represents the 5-95 percentile range. Observational data from Prochaska et al. 2011 (black symbols) and Tumlinson et al. 2011 (white circles). The Prochaska et al. 2011 data is split into three groups: $0.01L^* < L < 0.1L^*$, $0.1L^* < L < 1L^*$ and $L > 1L^*$. Only the relevant group is overplotted according to the luminosity of the shown galaxy.

APPENDIX A:

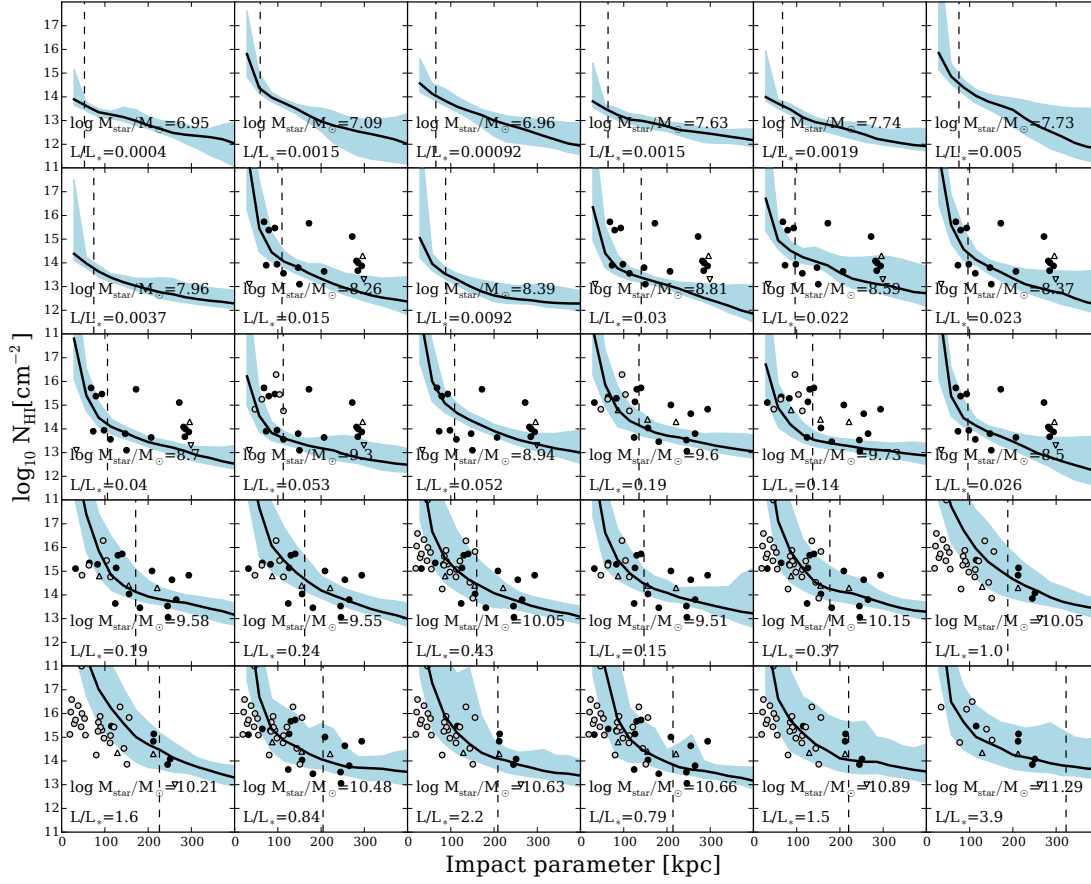


Figure A2. Mock sightline distributions of HI column density for the same 30 NIHAO galaxies as in fig. 2. Observational data from Prochaska et al. 2011 (black symbols) and Tumlinson et al. 2013 (white circles). The data is split into three groups: $L < 0.1L_*$, $0.1L_* < L < 1L_*$ and $L > 1L_*$. Only the relevant group is overplotted according to the luminosity of the shown galaxy.